



ELSEVIER

Contents lists available at ScienceDirect

Journal of the Mechanics and Physics of Solids

journal homepage: www.elsevier.com/locate/jmps

Mechanics of gradient nanostructured metals

Yin Zhang^a, Zhao Cheng^b, Ting Zhu^{c,*}, Lei Lu^{b,*}^a State Key Laboratory for Turbulence and Complex System, Department of Mechanics and Engineering Science, Peking University, Beijing 100871, China^b Shenyang National Laboratory for Materials Science, Institute of Metal Research, Chinese Academy of Sciences, Shenyang 110016, China^c Woodruff School of Mechanical Engineering, Georgia Institute of Technology, Atlanta, GA 30332, USA

ARTICLE INFO

Keywords:

Gradient nanotwinned Cu
 Strain gradient plasticity modeling
 Representative volume element
 Extra strength
 Back stress

ABSTRACT

The emergence of heterogeneous nanostructured materials (HNMs) offers exciting opportunities to achieve outstanding mechanical properties. Among these materials, gradient nanotwinned (GNT) Cu is a prominent class of HNMs, demonstrating superior strengths by gaining extra strengths compared to non-gradient counterparts. Its layered gradient structure provides a simplified quasi-one-dimensional model system for understanding the extra strengthening effects of structural gradients and resulting plastic strain gradients. This paper presents a comprehensive report for recent experimental and modeling studies on the mechanics of GNT Cu, covering advances in controlled material processing, back stress measurement, deformation field characterization, dislocation microstructure analysis, and strain gradient plasticity modeling. These studies unveil the spatiotemporal evolution of both plastic strain gradients and extra back stresses originating from structural gradients. Direct connections are established between the sample-level extra strength of GNT Cu and the synergistic strengthening effects induced by local nanotwin structures and their gradients. We emphasize the critical role of the size of the representative volume element in assessing the effects of plastic strain gradient and extra back stress. Moreover, lower-order strain gradient plasticity models are validated through experimental characterizations of GNT Cu, paving the way for future investigation into the mechanics of gradient nanostructured metals. Finally, we provide an outlook on research needs for understanding the mechanics of gradient nanostructured metals and, more broadly, HNMs, towards achieving exceptional mechanical properties.

1. Introduction

Heterogeneous nanostructured materials (HNMs) typically involve numerous sharp interfaces and/or strong structural gradients at the nanometer scale. They are widely pursued for achieving outstanding mechanical properties, including high yield strength, strain hardening, fracture toughness, and their combinations (Ji et al., 2023; Lu, 2016; Ma and Zhu, 2017; Wu and Zhu, 2017; Zhu et al., 2021; Zhu and Wu, 2023). Various structural designs have been explored, including bimodal, harmonic, lamellar, gradient, domain-dispersed, and hierarchical nanostructures (Ma and Zhu, 2017). Novel processing techniques, such as additive manufacturing (Gao et al., 2023; Ren et al., 2022; Wang et al., 2018) and electrodeposition (Cheng et al., 2022, 2018), enable facile control over local

This paper is dedicated to the special issue in honor of Prof. Wei Yang on the occasion of his 70th birthday.

* Corresponding authors.

E-mail addresses: ting.zhu@me.gatech.edu (T. Zhu), llu@imr.ac.cn (L. Lu).

<https://doi.org/10.1016/j.jmps.2024.105719>

Received 2 January 2024; Received in revised form 22 April 2024; Accepted 29 May 2024

Available online 30 May 2024

0022-5096/© 2024 Published by Elsevier Ltd.

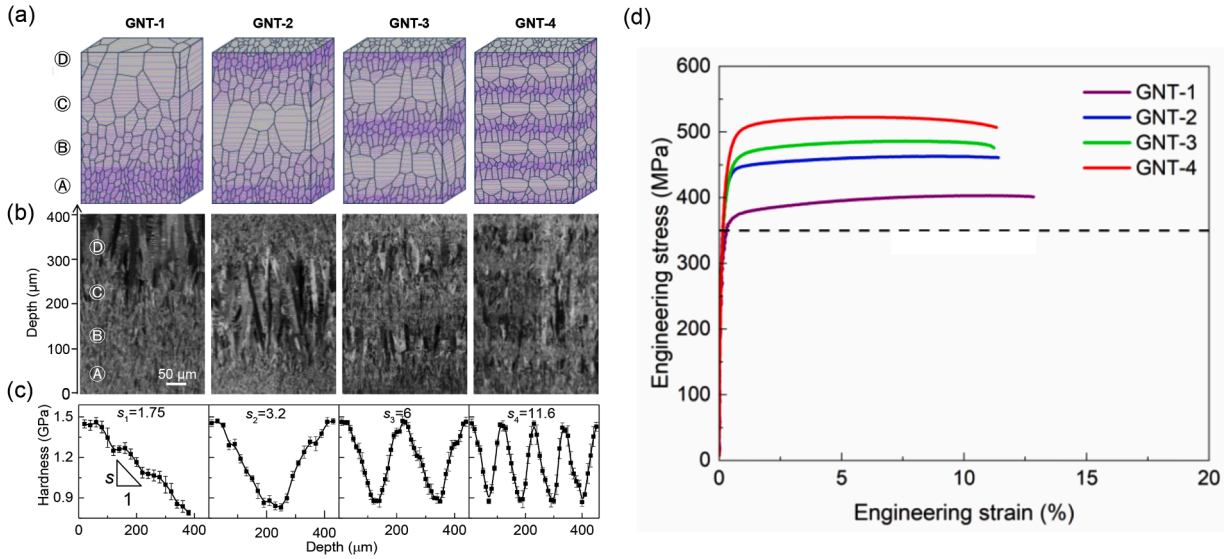


Fig. 1. Microstructures and mechanical properties of GNT Cu (Cheng et al., 2018). (a) Schematic illustration of GNT-1 to GNT-4. Through the sample thickness, gradient twin structures exhibit periodic, continuous variations of nanotwin thickness and grain sizes. Preferentially oriented nanometer-scale twin lamellas (with twin boundaries (TBs) represented by purple lines) are embedded within micrometer-scale columnar grains (with grain boundaries represented by blue lines). (b) Corresponding scanning electron microscopy (SEM) images. (c) Measured indentation hardness profiles through the sample thickness of GNT-1 to GNT-4. Each hardness curve is labeled with the corresponding hardness gradient (in the unit of GPa/mm). (d) Tensile stress-strain curves from GNT-1 to GNT-4. The dashed line indicates the estimated yield strength for GNT-1 to GNT-4 by the rule of mixtures.

nanostructures, facilitating the creation of highly heterogeneous nanostructures. The emerging mechanics effects of HNMs have been investigated through experimental and modeling characterizations, focusing on sample-level kinematic hardening and back stress strengthening (Zhu et al., 2021; Zhu and Wu, 2023). Significant effort is dedicated to elucidate how the macroscopic strength enhancement of HNMs arises from the synergistic strengthening effects of local heterogeneous nanostructures and their gradients (Cheng et al., 2022; Zhang et al., 2020). Understanding these mechanics effects is crucial for designing heterogeneous nanostructures to achieve exceptional mechanical performance.

Gradient nanotwinned (GNT) Cu is a prominent class of HNMs, demonstrating superior strengths by gaining extra strengths compared to non-gradient counterparts (Cheng et al., 2018). The controlled processing of GNT Cu via electrodeposition produces samples with periodically varying nanotwin thicknesses and different gradients through their cross section. These GNT Cu samples offer a simplified quasi-one-dimensional model system for understanding the extra strengthening effects of structural gradients and resultant plastic strain gradients. In this paper, we present a comprehensive report for recent experimental and modeling studies on the mechanics of GNT Cu (Bu et al., 2023; Cheng et al., 2022, 2023, 2018; Guo et al., 2024; Zhang et al., 2020). Notably, lower-order strain gradient plasticity models are developed and extensively validated through experimental characterizations of GNT Cu. The combined experimental and modeling results reveal the spatiotemporal evolution of both plastic strain gradients and extra back stresses originating from structural gradients. These results establish direct connections between the sample-level extra strength of GNT Cu and the synergistic strengthening effects induced by local nanotwin structures and their gradients. The critical role of the representative volume element size is emphasized in assessing the effects of plastic strain gradient and extra back stress on gradient nanostructured metals. Finally, we offer an outlook on the mechanics research of gradient nanostructured metals and, more broadly, HNMs.

2. Extra strengths of GNT Cu

Nanotwinned Cu with uniform twin thickness in the range of tens of nanometers usually exhibit high yield strengths from several hundred MPa up to about one GPa (Li et al., 2010; Lu et al., 2009a, 2009b; You et al., 2013; Zhu and Gao, 2012). To explore the strengthening effect of structural gradient, GNT Cu is processed by direct-current electrodeposition through stacking four components of homogeneous nanotwinned (HNT) Cu with increasing twin thickness from 28 nm to 70 nm (Fig. 1a), referred to as HNT-⊙ to HNT-⊙, respectively (Cheng et al., 2018). By tuning the processing conditions, GNT Cu exhibits a periodic, continuous variation of nanotwin thickness, close to a triangle wave, through the sample thickness (L) of around 400 μm. As shown in Fig. 1a-b, four types of GNT samples are obtained, with wavelengths of $2L$, L , $L/2$ and $L/4$, referred to as GNT-1 to GNT-4, respectively. Within each half period, the twin thickness changes from 28 nm to 70 nm in a nearly linear manner. Fig. 1c shows the corresponding triangle wave of measured indentation hardness (i.e., about three times yield strength) through the sample thickness of GNT-1 to GNT-4.

It is worth noting that the volume fraction (i.e., total thickness) of both hard layers with thin twins and soft layers with thick twins is nearly identical among GNT-1 to GNT-4 samples. Hence, the overall yield strengths of GNT-1 to GNT-4, when estimated by the rule of

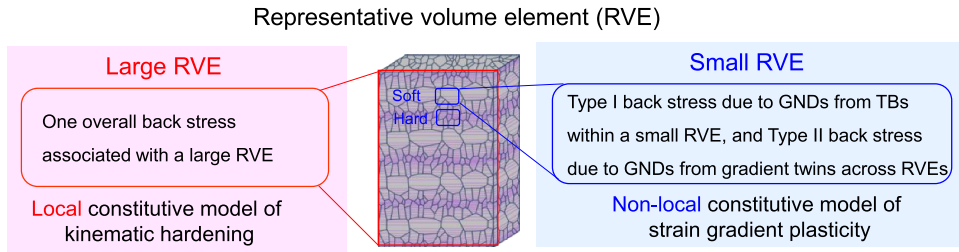


Fig. 2. A unified conceptual framework for the mechanics of gradient nanostructured metals, as applied to GNT Cu (Cheng et al., 2022). The direction of tensile loading is perpendicular to that of structural gradient.

mixtures from the yield strengths of four constituent HNT components, would be the same, as indicated by the dashed line in Fig. 1d. However, the experimentally measured stress-strain curves for GNT-1 to GNT-4 (Fig. 1d) show that their flow stresses surpass the rule-of-mixtures estimate, indicating substantial extra strengths in GNT Cu. Moreover, an increase in the nanotwin thickness gradient from GNT-1 to GNT-4 can result in a marked increase in the extra strength.

3. A unified conceptual framework

Fig. 2 presents a unified conceptual framework for the mechanics of gradient nanostructured metals, as applied to GNT Cu (Cheng et al., 2022). Two major microstructural length scales co-exist in GNT Cu: the wavelength of periodically varying nanotwin thickness (spanning hundreds of micrometers) and the thickness of individual nanotwin lamellae (in the tens of nanometers range). For constitutive modeling of GNT Cu, one needs to select a size for the representative volume element (RVE), which presumably corresponds to one of the aforementioned two length scales. As depicted in the red panel of Fig. 2, one approach to constitutive modeling involves employing a large RVE (red-boxed) that encompasses the entire GNT Cu sample. Incidentally, this large RVE is equivalent to the one containing at least one single period of gradient nanotwins, as the deformation field replicates across different periods under tensile loading through the sample thickness. With the gradient structure included in this large RVE, its strengthening effect can be captured using the local constitutive model of isotropic hardening and kinematic hardening. The former represents the hardening effect independent of tensile or compressive loading, while the latter accounts for the Bauschinger effect, i.e., asymmetry in the forward and reverse yield stress from a tension-compression test (Bower, 2009). Specifically, the flow stress associated with this large RVE can be partitioned into the effective stress and back stress. The effective stress represents non-directional, short-range resistance to dislocation glide, which typically arises from lattice friction and the local pinning by forest dislocation junctions. In contrast, the back stress is a result of directional, long-range resistance to dislocation glide, which originates from geometrically necessary dislocations (GNDs) (Ashby, 1970) that are generated to accommodate deformation incompatibility of heterogeneous microstructures within the large RVE. Hence, the back stress measured at the sample level corresponds to that of a large RVE in GNT Cu, reflecting the collective effects of GNDs from various types of heterogeneity inside this RVE.

In contrast to the large RVE, the blue panel in Fig. 2 presents an alternative approach to constitutive modeling by a small RVE (blue-boxed). Each small RVE encompasses a local region of nanotwins with approximately uniform thickness. The two adjacent small RVEs represent a relatively soft region containing thicker nanotwins and a relatively hard region containing thinner nanotwins, respectively. Under tensile loading through the sample thickness, the structural gradient and associated yield strength gradient across these adjacent RVEs induce a spatial gradient of plastic strain, resulting in an extra strengthening effect. This effect can be captured by the non-local constitutive model of strain gradient plasticity (Cheng et al., 2023) or the local constitutive model of kinematic hardening through an extra back stress. In essence, GNDs originating from the plastic strain gradient across adjacent RVEs act as one source of back stress in each small RVE. Meanwhile, it is important to recognize that a small RVE encompasses its internal microstructural heterogeneity, such as TBs between adjoining nanotwin lamellae. When GNDs arise to accommodate deformation incompatibility across the TBs, they serve as another source of back stress in each small RVE. Hence, the small RVE in GNT Cu typically involves two types of back stress: one due to structural heterogeneity within small RVEs (referred to type I back stress), and the other due to structural gradient across small RVEs (referred to as type II back stress). Establishing direct connections between the structural gradient, plastic strain gradient, type I and II back stresses in the small-RVE approach can provide a comprehensive understanding of the mechanics of GNT Cu. Furthermore, it is necessary to link the back stresses determined from the large-RVE and small-RVE approaches. Understanding these relationships is essential to the design and optimization of structural gradients and resultant strengthening effects.

To investigate the mechanics of GNT Cu, we have developed a phenomenological strain gradient plasticity (p-SGP) model (Zhang et al., 2020) as well as a mechanistic strain gradient plasticity (m-SGP) model (Cheng et al., 2022); the latter is further refined based on experimental characterizations of the spatiotemporal evolution of deformation fields in GNT Cu (Cheng et al., 2023). To illustrate the major differences between the p-SGP and m-SGP models, we briefly outline their applications in simulating uniaxial tensile responses of GNT-1 to GNT-4 Cu. In the p-SGP model, a gradient distribution of initial plastic flow resistance is prescribed through the normal cross section of each GNT model. With increased tensile loading, the plastic flow resistance at each material point (i.e., in a small RVE) increases with both local plastic strain and plastic strain gradient; the latter results in the extra strengthening effect of structural gradient. In contrast, the m-SGP model accounts for the distinct mechanics effects of different types of heterogeneous nanostructures,

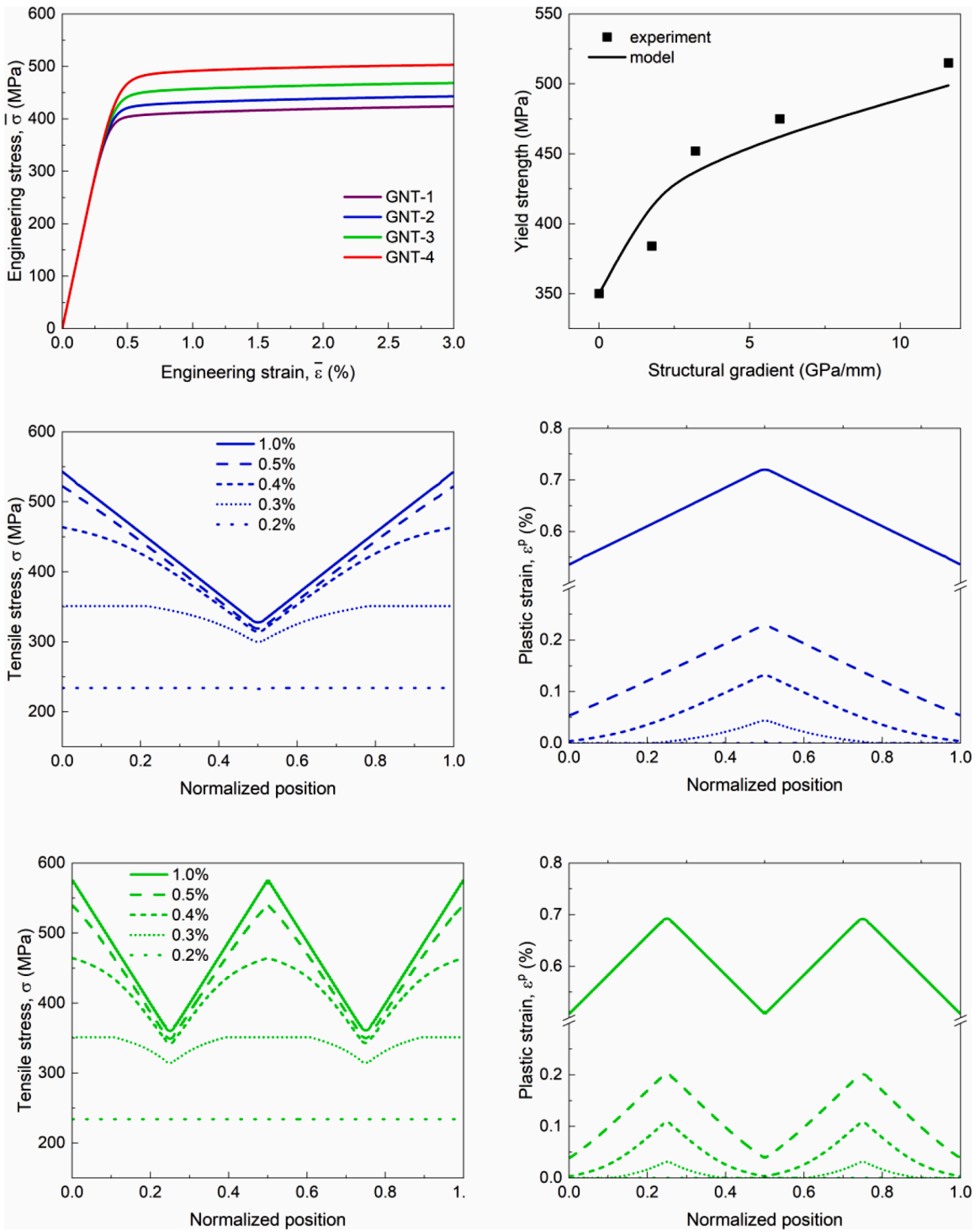


Fig. 3. Numerical results for uniaxial tension of GNT Cu from the p-SGP model (Zhang et al., 2020). (a) Simulated sample-level tensile stress-strain ($\bar{\sigma} - \bar{\epsilon}$) curves for GNT-1 to GNT-4. (b) Sample-level yield strength versus structural gradient (i.e., hardness gradient) for GNT-1 to GNT-4 from experimental measurements (squares) and modeling results (solid line). (c) Distributions of tensile stress as a function of position (normalized by the sample thickness) in the normal cross section of GNT-2 at different sample-level tensile strains. (d) Corresponding distributions of plastic strain for GNT-2. (e) Same as (c) but for GNT-3. (f) Corresponding distributions of plastic strain for GNT-3.

resulting in different plastic flow resistances in GNT Cu. Specifically, the total plastic flow resistance at each material point is taken as the sum of one effective stress and two back stresses (type I and II). The effective stress and back stress at the sample level (i.e., in a large RVE) represent the average of the local effective stresses and back stresses over all material points, respectively. Overall, while the p-SGP model captures the extra strengthening of structural gradient and enables efficient numerical simulations, the m-SGP model explicitly reveals the extra strengthening effects of gradient nanotwins and resultant plastic strain gradients. Hence, the m-SGP model provides a more comprehensive understanding of the mechanics effects of heterogeneous nanostructures, essential to the design and optimization of gradient nanostructured metals.

4. A phenomenological strain gradient plasticity model

In this Section, we first introduce the formulation of the p-SGP model, which incorporates the strengthening effect of plastic strain gradient into the classical J_2 flow theory, and then present the numerical results for GNT Cu (Zhang et al., 2020). Strain gradient plasticity has been extensively studied in the past (Aifantis, 1984; Ashby, 1970; Bassani, 2001; Fleck et al., 1994; Gudmundson, 2004; Lele and Anand, 2008; Niordson and Hutchinson, 2003; Nix and Gao, 1998). Inspired by Bassani's lower-order gradient theory of plasticity (Bassani, 2001), we develop a three-dimensional (3D) p-SGP model for GNT Cu by introducing a scalar measure of plastic strain gradients into a hardening rate relation. This eliminates the need for higher-order stress-related quantities and additional boundary conditions, simplifying the mathematical complexity. To highlight essential elements of the 3D p-SGP model, here we focus on the corresponding one-dimensional constitutive equations applied for uniaxial tensile deformation (Zhang et al., 2020). Specifically, the plastic strain rate $\dot{\varepsilon}^p$ at each material point (i.e., in a small RVE) is governed by a viscoplastic relation

$$\dot{\varepsilon}^p = \dot{\varepsilon}_0^p \left(\frac{\sigma}{\sigma_t} \right)^{1/m} \quad (1)$$

where $\dot{\varepsilon}_0^p$ is the reference plastic strain rate, σ_t is the total plastic flow resistance at this material point, and m is the strain rate sensitivity. The accumulated plastic strain at time t is given by $\varepsilon^p = \int_0^t \dot{\varepsilon}^p dt'$. Under applied tensile loading, σ_t increases with plastic strain and plastic strain gradient. The strengthening effect of plastic strain gradient is represented through the following hardening rate relation

$$\dot{\sigma}_t = h \dot{\varepsilon}^p \quad (2)$$

where the hardening rate coefficient h is

$$h = \frac{h_0}{1 + (\varepsilon^p/\varepsilon_1)^{n_1}} \left[1 + \frac{\kappa \sqrt{|\partial \varepsilon^p / \partial y|}}{1 + (\varepsilon^p/\varepsilon_2)^{n_2}} \right] \quad (3)$$

In Eq. (3), the term outside the square bracket represents the conventional hardening effect of plastic strain. That is, h_0 is the hardening rate constant, while ε_1 and n_1 control the nonlinear behavior of plastic strain hardening, resulting in two stages of strain hardening behavior, namely, the rate of plastic strain hardening in stage I ($\varepsilon^p < \varepsilon_1$) is much larger than that in stage II ($\varepsilon^p > \varepsilon_1$). In Eq. (3), the second term inside the square bracket represents the extra hardening effect due to plastic strain gradient $|\partial \varepsilon^p / \partial y|$. As such, the extra hardening rate due to plastic strain gradient scales with $\kappa \sqrt{\alpha} h_0$, where κ is a constant with the unit of $\sqrt{\text{m}}$, and $\kappa \sqrt{\alpha}$ serves as a dimensionless magnification factor of hardening rate arising from plastic strain gradient. In addition, ε_2 and n_2 are introduced to control the nonlinear behavior of the extra plastic strain hardening associated with plastic strain gradient. As a result, this extra hardening effect predominates when ε^p is less than ε_2 , but it decays quickly as ε^p increases above ε_2 .

To quantitatively represent the hardening effects of both the plastic strain and plastic strain gradient in GNT Cu, the parameter ε_2 should be much smaller than ε_1 , while an appropriate κ should be taken, such that $\kappa \sqrt{\alpha} h_0$ is much larger than h_0 . As a result, Eq. (3) effectively captures the two stages of extra hardening response arising from the plastic strain gradient in GNT Cu. Namely, a high hardening rate on the order of $\kappa \sqrt{\alpha} h_0$ predominates when ε^p is less than ε_2 , while a low hardening rate on the order of h_0 takes over when ε^p becomes greater than ε_2 . This two-stage hardening behavior is characteristic of the experimentally measured stress-strain response of GNT Cu (Zhang et al., 2020) and implies the following dislocation strengthening effects in gradient structures. During the stage I of hardening induced by plastic strain gradients, GNDs quickly form to accommodate plastic strain gradients resulting from built-in strength gradients. These GNDs contribute to high hardening rates at small strains, reflecting strong strengthening effects of plastic strain gradients. In stage II, hardening due to plastic strain gradients slowly approaches saturation, resulting in significantly reduced hardening rates at large strains.

We employ the p-SGP model to simulate the uniaxial tension responses of GNT-1 to GNT-4, and obtain consistent simulation results through both direct numerical integration with MATLAB and finite element analysis with ABAQUS (Zhang et al., 2020). For each GNT model, its normal cross section is assigned with a gradient distribution of initial plastic flow resistance. Based on the experimentally measured hardness profiles of GNT-1 to GNT-4 samples (Fig. 1), triangle waves with different wavelengths and gradients are used to represent their initial plastic flow resistances. The numerical results in Fig. 3 show the evolution of distributions of tensile stress, plastic strain and plastic resistance with increasing load. We note that in this paper, the sample-level stress and strain are represented by symbols with an overbar, which indicates an average over local stresses and strains (as represented by symbols without an overbar) in the normal cross section of each GNT Cu sample.

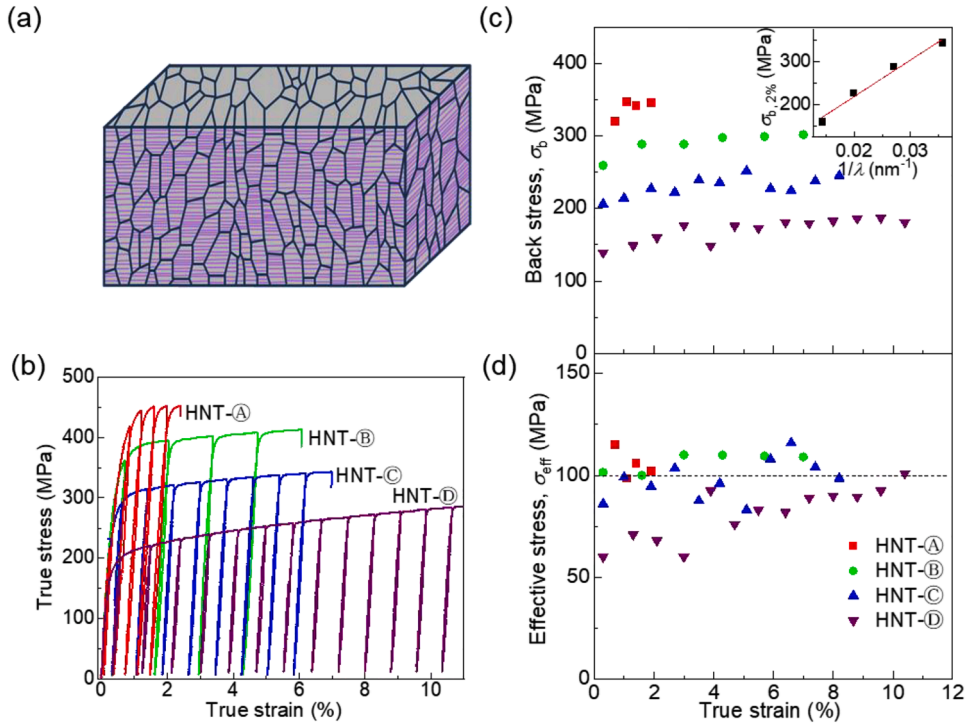


Fig. 4. Experimental results of HNT Cu (Cheng et al., 2022). (a) Schematic illustration of HNT-⊗. (b) Tensile loading-unloading stress-strain curves of HNT-⊕ to ⊗ samples. (c) Back stress σ_b versus tensile strain for HNT-⊕ to ⊗. Insert shows that the back stresses of HNT-⊕ to ⊗ at the applied strain of 2%, denoted as $\sigma_{b,2\%}$, follow a linear relationship with the reciprocal of twin thickness λ . (d) Same as (d) but for effective stress σ_{eff} . The dashed line indicates the saturated effective stress of 100 MPa.

In Fig. 3a, we plot the simulated sample-level tensile stress $\bar{\sigma}$ versus strain $\bar{\epsilon}$ curves for GNT-1 to GNT-4, which are close to the corresponding experimental results in Fig. 1c. The sample-level yield strength is defined as $\bar{\sigma}$ at $\bar{\epsilon} = 2\%$. In Fig. 3b, the predicted sample-level yield strength (solid line) is plotted as a function of structural gradient (i.e., hardness gradient), and it agrees with the corresponding experimental results for GNT-1 to GNT-4 (squares). The detailed results for GNT-1 to GNT-4 reveal the distributions of tensile stress and plastic strain as a function of position (normalized by sample thickness) in the normal cross section, demonstrating the progressive yielding in each type of GNT Cu as well as the extra strengthening induced by structural gradient by comparing different types of GNT Cu. Taking GNT-2 as an example, Figs. 3c and 3d show the distributions of tensile stress and plastic strain at different tensile strains $\bar{\epsilon}$, respectively. At low $\bar{\epsilon}$, the elastic response in the hard region containing thin twins gives a uniform distribution of tensile stress, while the plastic response in the soft region containing thick twins results in a gradient distribution of tensile stress. The plastic domain expands with increasing $\bar{\epsilon}$, reflecting the process of progressive yielding in the normal cross section. When $\bar{\epsilon}$ reaches 0.4%, progressive yielding has completed, so that the entire cross section becomes plastically yielded, as seen from Fig. 3d. When $\bar{\epsilon}$ increases to 0.5%, Fig. 3c shows that the distribution of tensile stress becomes almost linear. As $\bar{\epsilon}$ further increases, Figs. 3c and d show that the increasing tensile stress and plastic strain in the cross section remain linear distributions with opposite, but constant slopes. These distributions indicate the saturated extra hardening effect, which stems from a constant structural gradient leading to a constant saturated plastic strain gradient (Fig. 3d). In comparison, Figs. 3e and f show the distributions of tensile stress and plastic strain in the normal cross section of GNT-3 at different tensile strains $\bar{\epsilon}$, respectively. As GNT-2 and GNT-3 have the same sample thickness of about 400 μm , the gradient of plastic strain in GNT-3 (Fig. 3f) almost doubles that in GNT-2 (Fig. 3d) at the same load $\bar{\epsilon}$. It follows that the larger gradient of plastic strain in GNT-3 results in an upward shift of the tensile stress distribution (Fig. 3e) compared to GNT-2 (Fig. 3c), leading to the higher sample-level flow stress in GNT-3 relative to GNT-2 (Fig. 3a).

5. Mechanistic studies of strain gradient plasticity

This Section is focused on the combined experimental and modeling studies to establish direct connections between the structural gradient, plastic strain gradient, type I and II back stresses in the small-RVE approach for GNT Cu. Furthermore, direct linkages are established for the back stresses determined from the large-RVE and small-RVE approaches as well.

5.1. Experimental characterization of back stresses

As discussed in Section 3, a large RVE can encompass various types of heterogeneous nanostructures, each acting as a source of back

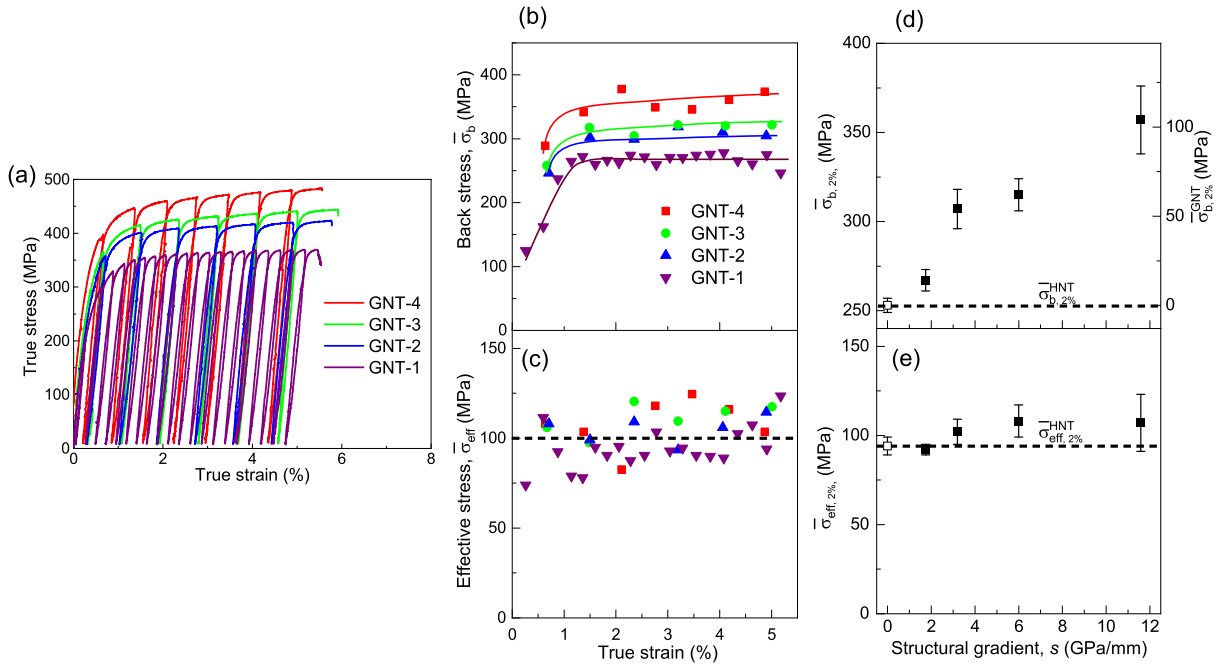


Fig. 5. Experimental results of microstructure, back stress and effective stress in GNT Cu (Cheng et al., 2022). (a) Tensile loading-unloading stress-strain curves of GNT-1 to GNT-4. (b) Sample-level back stress $\bar{\sigma}_b$ against tensile strain. (c) Same as (b) but for sample-level effective stress $\bar{\sigma}_{\text{eff}}$. (d) Sample-level back stress at the tensile strain 2%, denoted as $\bar{\sigma}_{b,2\%}$ (y axis on the left), versus structural gradient; also shown is the corresponding back stress induced by structural gradient, denoted as $\bar{\sigma}_{b,2\%}^{\text{HNT}}$ (y axis on the right). The open symbol and the horizontal dashed line represent the HNT-induced back stress $\bar{\sigma}_{b,2\%}^{\text{HNT}}$, which is estimated by the rule of mixtures from the back stresses of HNT-Ⓐ to Ⓔ. $\bar{\sigma}_{b,2\%}^{\text{HNT}}$ is the difference between $\bar{\sigma}_{b,2\%}$ and $\bar{\sigma}_{b,2\%}^{\text{HNT}}$. The error bars are evaluated from 3~5 measured values near the applied strain 2%. (e) Same as (d) but for the sample-level effective stress at the tensile strain 2%, denoted as $\bar{\sigma}_{\text{eff},2\%}$.

stress. In the case of GNT Cu, TBs serve as one type of heterogeneity. With increasing load, GNDs accumulate at TBs to accommodate the deformation incompatibility between adjoining nanotwin lamellae with different lattice orientations. These GNDs produce a back stress (type I) to oppose the operation of dislocation sources. Furthermore, the structural gradient of GNT Cu represents another type of heterogeneity. GNDs also accumulate to accommodate the deformation incompatibility between nanotwin lamellae with different thicknesses. These GNDs generate an extra back stress (type II) to impede the operation of dislocation sources. These two types of back stress in GNT Cu have been characterized through mechanical testing of HNT and GNT Cu samples (Cheng et al., 2022).

Specifically, we measure the back stresses originating from TBs using HNT Cu samples with different uniform twin thicknesses (Cheng et al., 2022). Four types of HNT Cu samples, referred to as HNT-Ⓐ, HNT-Ⓑ, HNT-Ⓒ and HNT-Ⓓ, respectively, are prepared by electrodeposition. From HNT-Ⓐ to HNT-Ⓓ, the average twin thickness increases from 28, 37, 50 to 70 nm, respectively, as schematically illustrated for HNT-Ⓐ in Fig. 4a. Considering that the stress-strain response of each HNT sample corresponds to that of a material point (excluding the gradient effect) in a GNT sample, we represent the sample-level stress and strain in HNT Cu by symbols without an overbar. Fig. 4b shows the tensile stress-strain curves with multiple unloading-reloading branches for HNT-Ⓐ to HNT-Ⓓ. For each sample, the tensile stress exhibits rapid increase at small tensile strain and then switches to slow increase when the tensile strain exceeds about 2%. Such a two-stage hardening response is also measured for GNT Cu. The tensile stress at the tensile strain 2%, denoted as $\sigma_{2\%}$, is taken as the yield strength for HNT Cu. From HNT-Ⓐ to Ⓓ, $\sigma_{2\%}$ decreases from 448, 392, 320 to 228 MPa, showing a strong dependence on the twin thickness in HNT Cu.

From multiple unloading-reloading branches in Fig. 4b, the back stress σ_b and effective stress σ_{eff} are determined as a function of tensile strain using Dickson's method (Dickson et al., 1984) for HNT-Ⓐ to HNT-Ⓓ, as shown in Figs. 4c and d, respectively. From HNT-Ⓓ to HNT-Ⓐ, σ_b increases markedly with decreasing twin thickness λ (Fig. 4c). For example, σ_b at the tensile strain 2%, denoted as $\sigma_{b,2\%}$, is 160 MPa in the softest HNT-Ⓓ with the largest λ of 70 nm, as compared with 346 MPa in the strongest HNT-Ⓐ with the smallest λ of 28 nm. The inset of Fig. 4c shows that $\sigma_{b,2\%}$ follows approximately a linear relationship with $1/\lambda$. In contrast, σ_{eff} exhibits a weak dependence on λ at low tensile strain and approaches a saturated value close to 100 MPa (Fig. 4d). There is no significant increase in σ_{eff} with increasing strain, except for HNT-Ⓓ whose σ_{eff} increases from ~60 MPa at small strain to the saturated value close to 100 MPa at the strain 8%. Altogether, the above results indicate that the back stress of HNT Cu at the tensile strain 2% is much higher than the corresponding effective stress and accounts for about 70% of the overall tensile stress. Furthermore, the twin thickness dependence of the overall tensile stress for HNT-Ⓐ to Ⓓ samples is caused mostly by that of the back stress, while the effective stress depends weakly on twin thickness.

Fig. 5 shows the experimental results of the effective stress and back stress in GNT Cu. From the tensile stress-strain ($\bar{\sigma} - \bar{\epsilon}$) curves with multiple unloading-reloading branches for GNT-1 to GNT-4 (Fig. 5a), the sample-level back stress $\bar{\sigma}_b$ versus tensile strain $\bar{\epsilon}$ is obtained (Fig. 5b). For each type of GNT Cu, $\bar{\sigma}_b$ at $\bar{\epsilon} = 2\%$, denoted as $\bar{\sigma}_{b,2\%}$, is high, accounting for about 75% of $\bar{\sigma}$; $\bar{\sigma}_b$ further increases by less than 10% with increasing $\bar{\epsilon}$ until failure. From GNT-1 to GNT-4, $\bar{\sigma}_b$ increases markedly with structural gradient. Particularly, $\bar{\sigma}_{b,2\%}$ of GNT-4 reaches 360 MPa, surpassing that of the strongest component HNT-⊙. This further demonstrates the strong extra strengthening effect associated with the back stress arising from structural gradient. In contrast, the sample-level effective stress $\bar{\sigma}_{\text{eff}}$, as shown in Fig. 5c, is much lower than $\bar{\sigma}_b$ for each type of GNT Cu. From GNT-1 to GNT-4, $\bar{\sigma}_{\text{eff}}$ exhibits a weak dependence on structural gradient and quickly reaches similar saturated values around 100 MPa at the tensile strain 2%.

To further correlate the back stress and effective stress with structural gradient, Fig. 5d shows the measured $\bar{\sigma}_{b,2\%}$ (see the left y axis) as a function of structural gradient s (i.e., hardness gradient) for GNT-1 to GNT-4. Based on the measured values of $\sigma_{b,2\%}$ from HNT-⊙ to HNT-⊙, we estimate $\bar{\sigma}_{b,2\%}$ as 253 MPa for GNT Cu by the rule of mixtures, which corresponds to $\bar{\sigma}_{b,2\%}$ in the limit of zero structural gradient (indicated by the dashed line in Fig. 5d). For GNT-1 to GNT-4, the extra back stress due to structural gradient at the applied strain 2%, $\bar{\sigma}_{b,2\%}^{\text{GNT}}$, is determined from the difference between the measured $\bar{\sigma}_{b,2\%}$ and its estimate of 253 MPa by the rule of mixtures. As shown in Fig. 5d (see the right y axis), $\bar{\sigma}_{b,2\%}^{\text{GNT}}$ increases markedly with the structural gradient s from GNT-1 to GNT-4. In contrast, Fig. 5e shows the measured effective stress at the tensile strain 2%, $\bar{\sigma}_{\text{eff},2\%}$, as a function of structural gradient s for GNT-1 to GNT-4. Based on the measured values of $\sigma_{\text{eff},2\%}$ from HNT-⊙ to HNT-⊙, we estimate $\bar{\sigma}_{\text{eff},2\%}$ as 94 MPa for GNT Cu by the rule of mixtures, which corresponds to $\bar{\sigma}_{\text{eff},2\%}$ in the limit of zero structural gradient (indicated by the dashed line in Fig. 5e). The measured $\bar{\sigma}_{\text{eff},2\%}$ of GNT-1 to GNT-4 is only slightly higher than the estimated value by the rule of mixtures, indicative of its weak dependence on structural gradient. Altogether, the above results show that the extra strength of GNT Cu, $\bar{\sigma}_{b,2\%}$, is caused primarily by the extra back stress $\bar{\sigma}_{b,2\%}^{\text{GNT}}$ due to structural gradient.

5.2. A mechanistic strain gradient plasticity model

Based on the experimental results of the back stresses in both HNT and GNT Cu (Section 5.1), we develop a m-SGP model (Cheng et al., 2022) to explicitly account for the type I and II back stresses associated with small RVEs and further connect them with the sample-level back stress in GNT-1 to GNT-4 (i.e., large RVEs). Consistent with the p-SGP model in Section 4, we apply the 3D m-SGP model to simulate the uniaxial tensile deformation of GNT Cu. Specifically, the plastic strain rate $\dot{\epsilon}^p$ at each material point (i.e., a small RVE) is governed by a viscoplastic relation

$$\dot{\epsilon}^p = \dot{\epsilon}_0^p \left(\frac{|\sigma - \sigma_b|}{\sigma_{\text{eff}}} \right)^m \text{sgn}(\sigma - \sigma_b) \quad (4)$$

where σ_{eff} is the effective stress and σ_b is the total back stress at this material point. In contrast to Eq. (1), the total plastic flow resistance σ_t at this material point is divided into σ_{eff} and σ_b

$$\sigma_t = \sigma_{\text{eff}} + \sigma_b \quad (5)$$

Then σ_b is further partitioned into two components

$$\sigma_b = \sigma_b^{\text{HNT}} + \sigma_b^{\text{GNT}} \quad (6)$$

where σ_b^{HNT} is the type I back stress originating from homogeneous nanotwins, and σ_b^{GNT} is the type II back stress due to the structural gradient in gradient nanotwins. To capture the nonlinear evolution of σ_b^{HNT} and σ_b^{GNT} , we represent the rate of change of σ_b^{HNT} as

$$\dot{\sigma}_b^{\text{HNT}} = c^{\text{HNT}} (\sigma_{\text{sat}}^{\text{HNT}} - \sigma_b^{\text{HNT}}) \dot{\epsilon}^p \quad (7)$$

where $\sigma_{\text{sat}}^{\text{HNT}}$ is the saturated value of the back stress from homogeneous nanotwins and c^{HNT} is the associated coefficient. Based on our experimental measurements in Section 5.1, $\sigma_{\text{sat}}^{\text{HNT}}$ is proportional to the inverse of twin thickness $\sigma_{\text{sat}}^{\text{HNT}}$. Hence, $\sigma_{\text{sat}}^{\text{HNT}}$ is expressed as

$$\sigma_{\text{sat}}^{\text{HNT}} = \beta \frac{\mu b}{\lambda} \quad (8)$$

where β is a constant coefficient, μ is the shear modulus and b is the Burgers vector length. Similarly, we represent the rate of change of σ_b^{GNT} as

$$\dot{\sigma}_b^{\text{GNT}} = c^{\text{GNT}} (\sigma_{\text{b,sat}}^{\text{GNT}} - \sigma_b^{\text{GNT}}) \dot{\epsilon}^p \quad (9)$$

where $\sigma_{\text{sat}}^{\text{GNT}}$ is the saturated value of the back stress originating from the structural gradient and c^{GNT} is the associated coefficient. When the m-SGP was initially developed, no experimental data were available on the distribution of plastic strain in GNT Cu, so that the distribution of $\sigma_{\text{sat}}^{\text{GNT}}$ could not be deduced. Hence, we assumed a simplified relation for $\sigma_{\text{sat}}^{\text{GNT}}$ that solely relies on the GNDs due to the structural gradient in GNT Cu, and expressed $\sigma_{\text{sat}}^{\text{GNT}}$ as

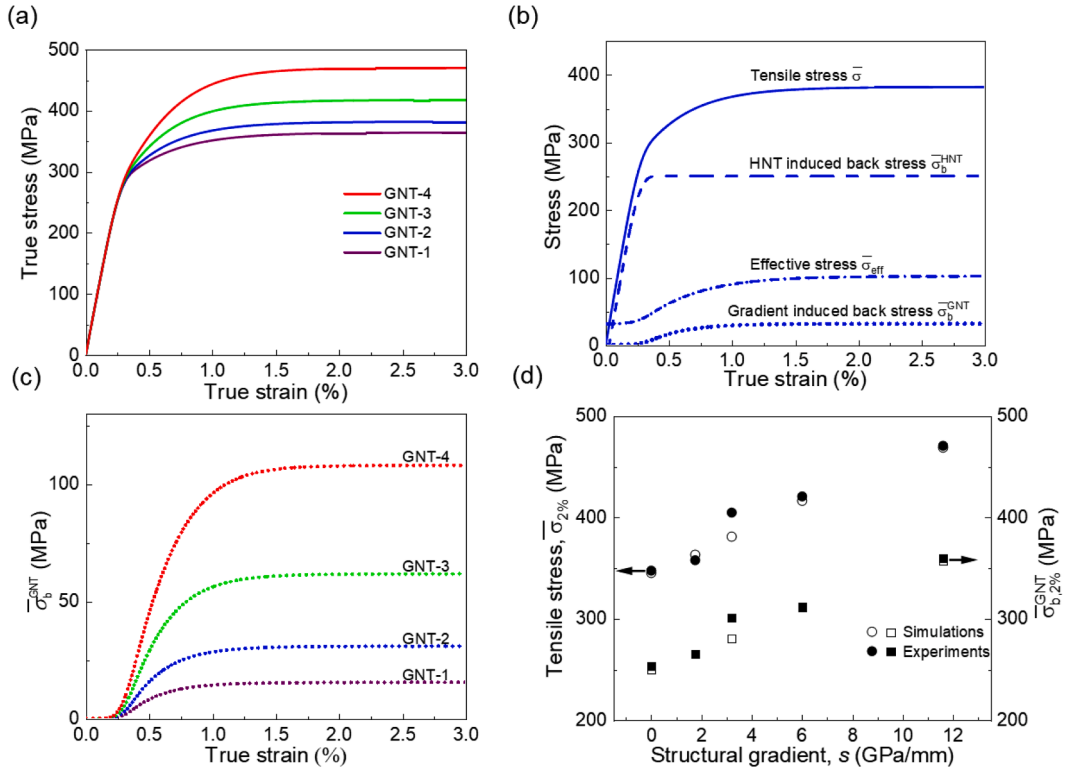


Fig. 6. Numerical results for the sample-level stress-strain responses of GNT Cu under uniaxial tension from the m-SGP model (Cheng et al., 2022). (a) Sample-level stress-strain curves of GNT-1 to GNT-4. (b) Sample-level tensile stress $\bar{\sigma}$ for GNT-2, along with the corresponding effective stress $\bar{\sigma}_{\text{eff}}$, back stress associated with HNT $\bar{\sigma}_b^{\text{HNT}}$, and extra back stress arising from structural gradient $\bar{\sigma}_b^{\text{GNT}}$. (c) Sample-level extra back stress arising from structural gradient $\bar{\sigma}_b^{\text{GNT}}$ against applied tensile strain for GNT-1 to GNT-4. (d) Comparison between experimental and numerical results of the sample-level tensile stress $\bar{\sigma}_{2\%}$ and back stress $\bar{\sigma}_{b,2\%}$ at $\bar{\epsilon} = 2\%$ versus structural gradient.

$$\sigma_{b,\text{sat}}^{\text{GNT}} = \mu b L \rho_G^{\text{GNT}} \quad (10)$$

where ρ_G^{GNT} is the density of GNDs resulting from the structural gradient and resultant plastic strain gradient, and L is the characteristic length of GNDs associated with the structural gradient. In addition, ρ_G^{GNT} is given by

$$\rho_G^{\text{GNT}} = \frac{|\nabla \varepsilon^p|}{b} \quad (11)$$

where $|\nabla \varepsilon^p|$ represents the magnitude of the gradient of tensile plastic strain ε^p . On the other hand, σ_{eff} evolves with the density of statistically stored dislocations (SSDs), which increases with ε^p in a nonlinear manner (Cheng et al., 2022).

Fig. 6 shows the numerical results of uniaxial tension of GNT Cu based on the m-SGP model (Cheng et al., 2022). In Fig. 6a, we present the simulated tensile stress-strain ($\bar{\sigma} - \bar{\epsilon}$) curves for GNT-1 to GNT-4, which are close to the experimental results in Fig. 5c. Taking GNT-2 as an example, Fig. 6b shows the corresponding responses of sample-level tensile stress $\bar{\sigma}$, effective stress $\bar{\sigma}_{\text{eff}}$, back stress associated with HNT $\bar{\sigma}_b^{\text{HNT}}$, and back stress arising from structural gradient $\bar{\sigma}_b^{\text{GNT}}$ against $\bar{\epsilon}$. It is seen that $\bar{\sigma}_b^{\text{HNT}}$ provides a significant contribution to $\bar{\sigma}$ relative to $\bar{\sigma}_{\text{eff}}$ and $\bar{\sigma}_b^{\text{GNT}}$. However, $\bar{\sigma}_b^{\text{GNT}}$ increases substantially with the increasing structural gradient in GNT Cu (Fig. 6c), while $\bar{\sigma}_b^{\text{HNT}}$ and $\bar{\sigma}_{\text{eff}}$ remain relatively constant, thereby underscoring the effect of the structural gradient on increasing $\bar{\sigma}_b^{\text{GNT}}$ and $\bar{\sigma}$. Fig. 6d shows a close agreement between the simulated and experimental results of $\bar{\sigma}_{2\%}$ and $\bar{\sigma}_{b,2\%}$ as a function of the structural gradient (i.e., hardness gradient) in GNT Cu. This comparison not only validates the numerical simulations from the m-SGP model, but also underscores that the extra strengthening of GNT Cu predominantly arises from the plastic strain gradient and associated extra back stress.

Fig. 7 shows the simulated distributions of tensile stress σ , plastic strain ε^p , HNT-induced back stress σ_b^{HNT} , and GNT-induced extra back stress σ_b^{GNT} in the normal cross section of GNT-2 at different applied tensile strains. The numerical results of tensile stress in Fig. 7a and plastic strain in Fig. 7b from the m-SGP model are close to the corresponding results in Figs. 3c and 3d from the p-SGP model, respectively. Their small quantitative differences arise mainly due to variations of the experimental stress-strain curves between Figs. 3a and 5a for GNT-Cu, which are caused by the effect of reduced loading rate as well as repeated unloading and reloading for samples in Fig. 5a. Additionally, Figs. 7c and 7d show the distributions of σ_b^{HNT} and σ_b^{GNT} in GNT-2, demonstrating the distributions of

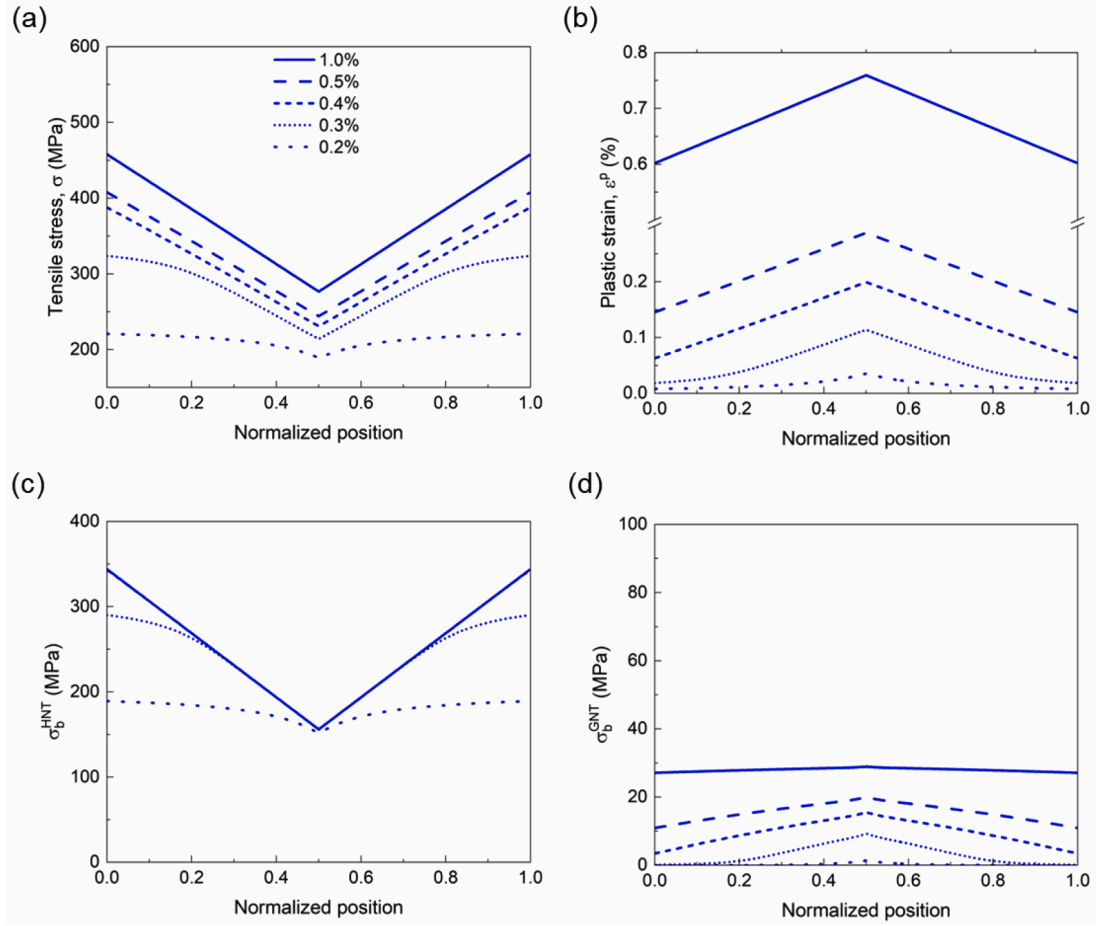


Fig. 7. Numerical results for the spatial distributions of tensile stress, plastic strain and back stress in GNT-2 under uniaxial tension from the m-SGP model (Cheng et al., 2022). (a) Distributions of tensile stress σ in the normal cross section at different applied tensile strains. (b) Corresponding distributions of plastic strain ε^p . (c) Corresponding distributions of HNT-induced back stress σ_b^{HNT} . The σ_b^{HNT} curves overlap for the applied tensile strain of 0.4%, 0.5% and 1.0%. (d) Corresponding distributions of extra back stress σ_b^{GNT} arising from the structural gradient of GNT-2.

back stress due to HNTs and structural gradients in GNTs, respectively. It is important to recognize that the sample-level back stresses $\bar{\sigma}_b^{\text{HNT}}$ and $\bar{\sigma}_b^{\text{GNT}}$ at an applied tensile strain in Fig. 6b correspond to the respective average over σ_b^{HNT} and σ_b^{GNT} in the normal cross section of GNT-2. Moreover, the directly measured back stress at the sample level from experiment, as shown in Fig. 5b, corresponds to the sum of $\bar{\sigma}_b^{\text{HNT}}$ and $\bar{\sigma}_b^{\text{GNT}}$. These results provide in-depth information on the spatiotemporal evolution of type I and type II back stresses arising from heterogeneous nanostructures in GNT Cu. The gradient of plastic strain in Fig. 7b becomes saturated when $\bar{\varepsilon}$ is above 0.5%, while the plastic strain continues to increase with $\bar{\varepsilon}$. As a result, the distribution of σ_b^{GNT} approaches a saturated uniform distribution in Fig. 7d, as seen from the nearly constant value of σ_b^{GNT} when $\bar{\varepsilon} = 1\%$. Achieving a saturated gradient of plastic strain in GNT Cu can be rationalized through a scaling analysis of plastic strain gradient (Zhang et al., 2020), as indicated by a constant structural gradient of nanotwins in GNT-1 to GNT 4. However, the saturated uniform distribution of σ_b^{GNT} arises due to the formulation of the saturated back stress by Eqs. (9-11) in the m-SGP model. As discussed below, this formulation should be revised to give a saturated non-uniform distribution of σ_b^{GNT} , based on experimental characterizations of the spatial distribution of plastic strain in GNT Cu.

5.3. Experimental characterization of gradient distributions of plastic strain

Numerical simulations based on the m-SGP model in Fig. 7 reveal the sample-level strengthening effects of structural gradient, as well as the distributions of plastic strain and HNT and GNT-induced back stresses in the cross section of GNT-1 to GNT-4. To improve the m-SGP model, it is desirable to obtain direct experimental information on the spatial distribution of plastic strain, which can be used to validate the corresponding numerical simulations. To achieve this, we use full-field strain mapping to characterize the spatial distribution of lateral strain in the transverse cross section of GNT-1 to GNT-4 samples under uniaxial tension (Cheng et al., 2023). Due to Poisson's effect, the distribution of lateral strain in the transverse cross section of an unloaded sample can be used to derive the distribution of tensile plastic strain within the normal cross section of each GNT sample.

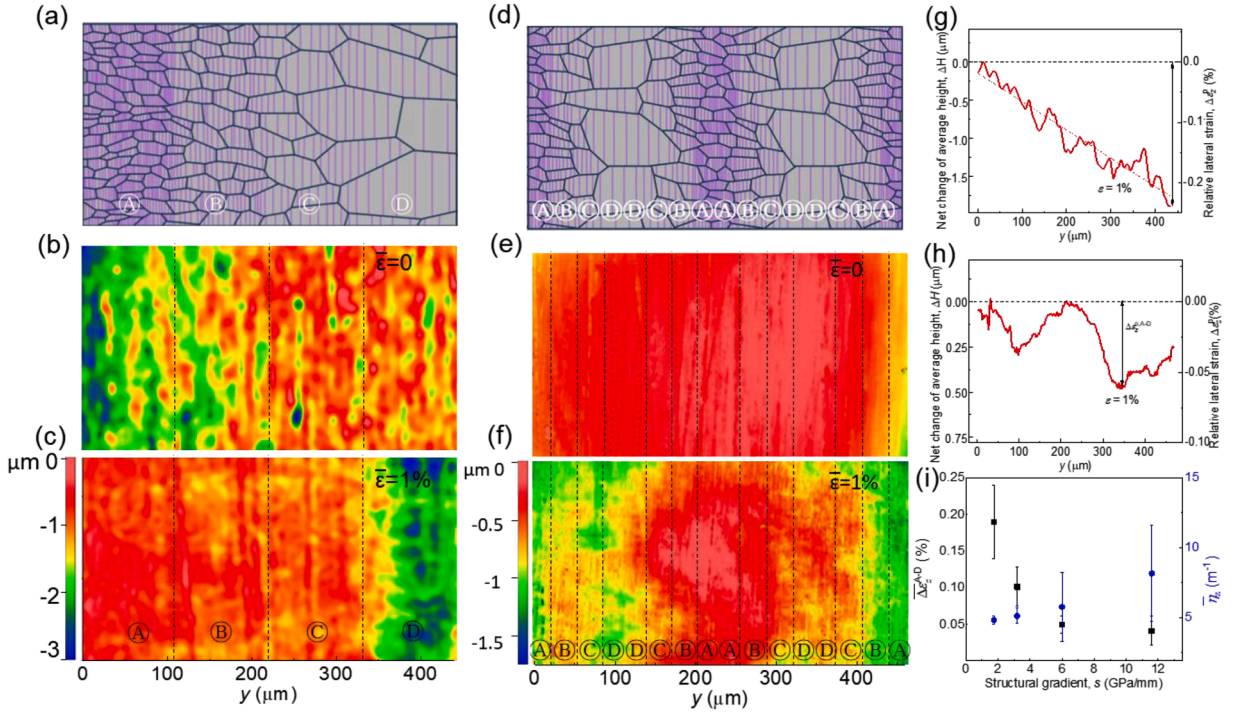


Fig. 8. Experimental results for the distributions of lateral strain in the transverse cross section of GNT-1 and GNT-3 (Cheng et al., 2023). (a) Schematic through the sample thickness of GNT-1. (b) Measured height contour on the lateral surface of GNT-1 without applied tensile strain, $\bar{\varepsilon} = 0$. (c) Same as (b) but for $\bar{\varepsilon} = 1\%$. (d) Schematic through the sample thickness of GNT-3. (e) Same as (b), but for GNT-3. (f) Same as (c), but for GNT-3. (g) Net change of the average height $|\Delta H|$ on the lateral surface of GNT-1 at $\bar{\varepsilon} = 1\%$ relative to that at $\bar{\varepsilon} = 0$, where the smallest $|\Delta H|$ is set zero as the reference point (left axis), and the corresponding distribution of average relative lateral strain (right axis). (h) Same as (g), but for GNT-3. (i) Difference in the average lateral strain between components \textcircled{A} and \textcircled{D} (left y axis) and lateral strain gradient (right y axis) against structural gradient from GNT-1 to GNT-4.

In the experiment, a tensile GNT specimen is put under a confocal laser scanning microscopy with a planar resolution of 120 nm and a height resolution of 10 nm to measure the height of the lateral surface. As an example of measured lateral strain distributions, Fig. 8a illustrates the schematic of gradient nanotwins in GNT-1. Fig. 8b shows the lateral surface height map of as-prepared GNT-1 (i.e., the applied tensile strain $\bar{\varepsilon} = 0$), which is uneven with small, gradual changes. Such unevenness arises from mechanical polishing. In contrast, the lateral surface height decreases markedly from the strongest end with the thinnest nanotwins (layer \textcircled{A} in Fig. 1a) to the weakest end with the thickest nanotwins (layer \textcircled{D} in Fig. 1a) after tensile deformation up to $\bar{\varepsilon} = 1\%$ (Fig. 8c). The net change of the average height ΔH at each y position is obtained by subtracting the average height profile at $\bar{\varepsilon} = 1\%$ from that at $\bar{\varepsilon} = 0$. Fig. 8g shows that the absolute value of $|\Delta H|$ increases linearly with y , indicating a gradient distribution of lateral strain $|\Delta \varepsilon_z^p|$ (along the lateral z direction). The lateral plastic strain difference $|\Delta \varepsilon_z^{p,A-D}|$ is estimated from the lateral strain at $y = 60$ and $380 \mu\text{m}$, which corresponds to the middle of layer \textcircled{A} and \textcircled{D} , respectively. The average lateral strain difference $|\overline{\Delta \varepsilon_z^{p,A-D}}|$ of GNT-1 reaches 0.19%, and the average lateral plastic strain gradient $|\overline{\nabla \varepsilon_z^p}|$ is estimated as 4.8 m^{-1} .

For comparison, Fig. 8d depicts the schematic of GNT-3. While the as-prepared GNT-3 sample exhibits a relatively smooth lateral surface (Fig. 8e), the height profile on the lateral surface becomes wavy at $\bar{\varepsilon} = 1\%$ (Fig. 8f). The net change in the average height ΔH at $\bar{\varepsilon} = 1\%$ is displayed in Fig. 8h. ΔH shows a dual-triangle wave along the y direction. Like GNT-1, both $|\Delta H|$ and $|\Delta \varepsilon_z^p|$ in GNT-3 display gradient distributions. However, the average $|\overline{\Delta \varepsilon_z^{p,A-D}}|$ for GNT-3 at $\bar{\varepsilon} = 1\%$ is only 0.05%, which is about one quarter of that for GNT-1. The average lateral plastic strain gradient $|\overline{\nabla \varepsilon_z^p}|$ of GNT-3 reaches 5.8 m^{-1} , which is 21% higher than that of GNT-1.

Fig. 8i shows the experimentally measured results of $|\overline{\Delta \varepsilon_z^{p,A-D}}|$ (left y axis) and $|\overline{\nabla \varepsilon_z^p}|$ (right y axis) against structural gradient from GNT-1 to GNT-4. It is seen that $|\overline{\Delta \varepsilon_z^{p,A-D}}|$ decreases rapidly from 0.19% to 0.04% when the structural gradient increases from 1.75 (GNT-1) to 11.6 GPa/mm (GNT-4). However, $|\overline{\nabla \varepsilon_z^p}|$ shows an opposite trend, increasing from 4.8 m^{-1} for GNT-1 to 8.2 m^{-1} for GNT-4. Although the structural gradient increases by a factor of about seven, the lateral strain gradient $|\overline{\nabla \varepsilon_z^p}|$ of GNT-4 is only twice that of GNT-1. This difference suggests that the increase of the lateral plastic strain gradient, and accordingly the increase of the plastic strain gradient along the tensile loading direction, is reduced with increasing structural gradient, which is largely due to a substantial

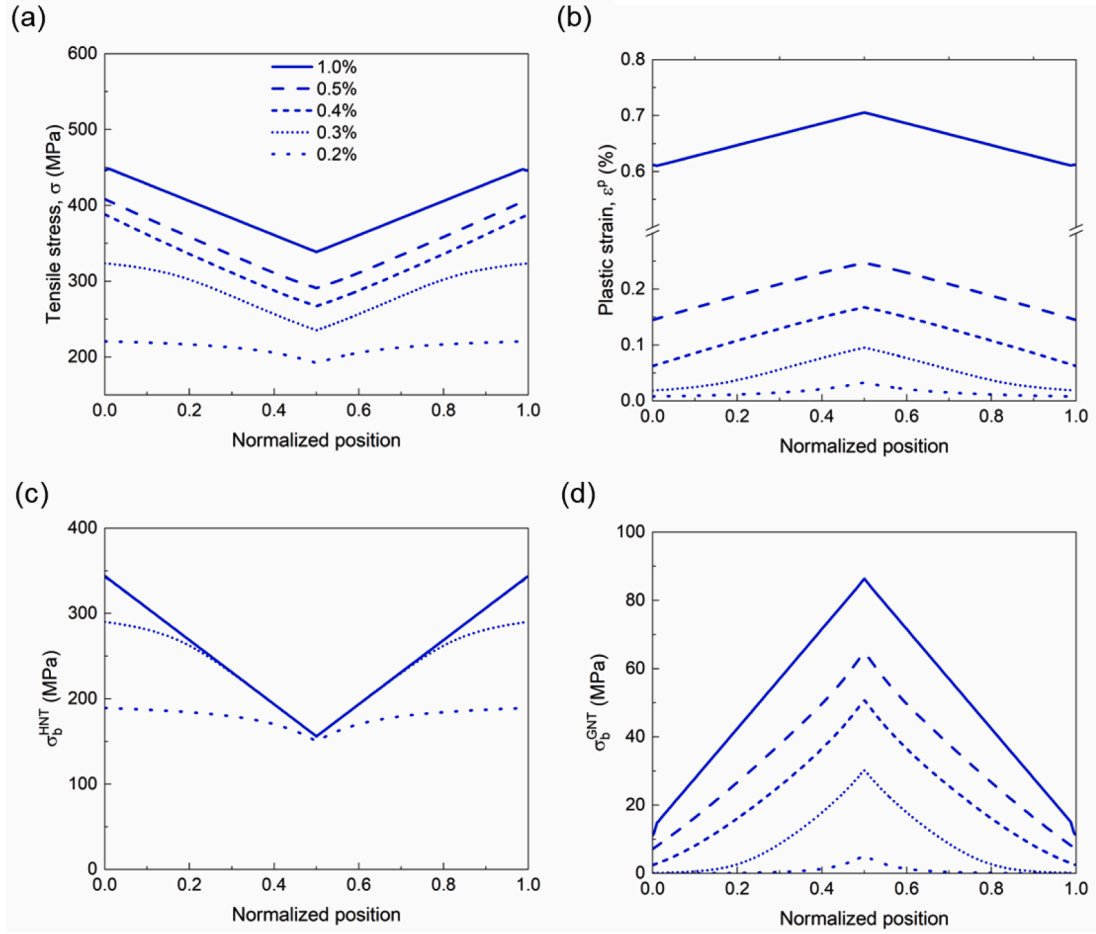


Fig. 9. Numerical results for the spatial distributions of tensile stress, plastic strain and back stress in GNT-2 under uniaxial tension from the improved m-SGP model (Cheng et al., 2023). (a) Distributions of tensile stress σ in the normal cross section at different applied tensile strains. (b) Corresponding distributions of plastic strain ε^p . (c) Corresponding distributions of HNT-induced back stress σ_b^{HNT} . The σ_b^{HNT} curves overlap for the applied tensile strain of 0.4%, 0.5% and 1.0%. (d) Corresponding distributions of extra back stress σ_b^{GNT} arising from the structural gradient of GNT-2, which contrast with those in Fig. 7(d).

reduction in $|\Delta\varepsilon_z^{\text{p,A-D}}|$. These results imply a non-uniform distribution of the saturated extra back stresses associated with the structural gradient in the sample cross section, which is at variance with the assumption of the uniform saturated extra back stress in the m-SGP model. This discrepancy is addressed by an improved m-SGP model, as shown in Section 5.4.

5.4. An improved m-SGP model

The m-SGP model in Section 5.2 explicitly accounts for the contributions of effective stress and back stress to plastic resistance. Based on experimental measurements of sample-level effective stresses and back stresses in HNT and GNT Cu, a term representing the type II back stress due to structural gradient σ_b^{GNT} is employed to reflect the extra strengthening effect of plastic strain gradient. The nonlinear evolution of σ_b^{GNT} with increasing load is characterized by a rate relation of σ_b^{GNT} given by Eq. (9). Correspondingly, σ_b^{GNT} reaches a saturated value, denoted as $\sigma_{b,\text{sat}}^{\text{GNT}}$, with increasing load at each point in the sample cross section. Since $\sigma_{b,\text{sat}}^{\text{GNT}}$ is assumed to be a constant independent of both twin thickness and grain size, a uniform distribution of saturated σ_b^{GNT} is predicted in the normal cross section of each GNT sample. However, experimental measurements in Section 5.3 reveal a decrease in $|\Delta\varepsilon_z^{\text{p,A-D}}|$ with increasing structural gradient. These results imply a non-uniform distribution of $\sigma_{b,\text{sat}}^{\text{GNT}}$, which is at variance with the assumption of the m-SGP model regarding a uniform distribution of σ_b^{GNT} in the normal cross section of each GNT sample.

To address the above issue, we improve the m-SGP model by incorporating the grain size dependence of $\sigma_{b,\text{sat}}^{\text{GNT}}$ (Cheng et al., 2023). Considering that the grain size increases with the nanotwin thickness in GNT Cu, we express $\sigma_{b,\text{sat}}^{\text{GNT}}$ by revising Eq. (10) as

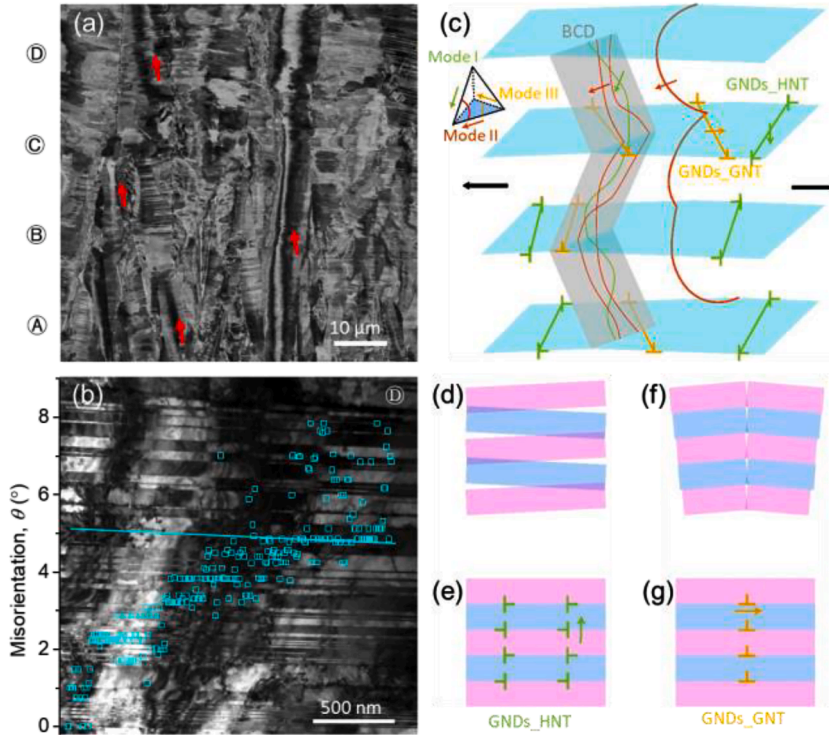


Fig. 10. Deformation mechanisms in GNT Cu (Cheng et al., 2022). (a) BCDs (indicated by red arrows) in the SEM image of a GNT-4 sample at $\bar{\epsilon} = 1\%$. (b) TEM image of a BCD in component ③ of GNT-4. Squares represent points where the local crystal orientation was measured to estimate the lattice misorientation and associated GND density along a twin lamella as indicated by a solid line. (c) Schematic illustration of dislocation structures in GNT Cu developed during plastic deformation under tensile loading (indicated by black arrows), based on TEM results. Dislocations of mode I, II and III are represented by green, brown and orange lines, respectively, and the corresponding Burgers vectors are shown on a Thompson tetrahedron. (d) Incompatible deformation (e.g., opening and overlap) between adjacent nanotwins (indicated by pink and blue layers) without mutual constraints in an HNT structure, and (e) accumulation of GNDs_{HNT} due to mutual constraints between adjacent nanotwins. (f) Incompatible deformation (e.g., opening) without deformation continuity requirement, as induced by sample-level plastic strain gradient resulting from structural gradient in a GNT structure, and (g) accumulation of GNDs_{GNT} to satisfy the requirement of deformation compatibility.

$$\sigma_{b,sat}^{GNT} = \kappa \mu b d \rho_G^{GNT} \quad (12)$$

where κ is a dimensionless parameter. Eq. (12) indicates that $\sigma_{b,sat}^{GNT}$ increases linearly with the grain size d and GND density ρ_G^{GNT} . Taking GNT-2 as an example, the corresponding numerical results of tensile stress (Fig. 9a), plastic strain (Fig. 9b), and σ_b^{HNT} (Fig. 9c) from the improved m-SGP model closely match the corresponding results in Figs. 7a, b and c from the original m-SGP model, respectively. However, Fig. 9d shows the non-uniform distributions of σ_b^{GNT} , which differ markedly the corresponding results in Fig. 7d.

The extra strengthening effect of GNT Cu was initially thought to be controlled by the plastic strain gradient and associated GND density, implying that a higher GND density leads to a higher extra back stress and thus a more pronounced extra strengthening effect. However, our experimental results for the gradient distribution of plastic strain indicate that a uniform distribution of plastic strain gradient and accordingly GND density in each type of GNT Cu can result in different local extra back stresses in the sample cross section. These findings suggest that the material length scale such as grain size, along with nanotwin thickness gradient, can influence local extra back stresses (type II) in the sample cross section, collectively determining the sample-level extra stress of GNT Cu. Consequently, the gradient distribution of grain size in each type of GNT Cu yields increased extra back stress from components ① to ③, thereby reducing differences in tensile flow stress and plastic strain across the components. This implies that plastic deformation incompatibility in GNT Cu can be reduced due to the gradient distribution of local extra stress. Hence, increasing the grain size and its gradient while maintaining the same nanotwin thickness gradient might be an effective strategy for further tuning the strength-ductility combination in GNT Cu.

5.5. Mechanistic underpinnings

To determine the dislocation mechanism responsible for the extra back stress associated with the structural gradient in GNT Cu, we conduct SEM and transmission electron microscopy (TEM) analyses of deformed HNT and GNT samples (Cheng et al., 2022). An unusual type of heterogeneous dislocation structure, in the form of bundles of concentrated dislocations (BCDs), is found to only

develop in deformed GNT Cu, not HNT Cu. The density of GNDs is estimated from TEM orientation mapping, showing the accumulation of GNDs in BCDs for accommodating the gradients of plastic strain. These GNDs can produce the extra back stress in GNT Cu.

Fig. 10a shows the SEM image of BCDs inside columnar grains in GNT-4 at $\bar{\epsilon} = 1\%$. These BCDs appear as long contrast strips aligned with the direction of twin thickness gradient. The BCD width along the horizontal direction increases from component ① to ④, ranging from 0.3 to 1.5 μm . The number fraction of grains with BCDs increases from 15% to 45%, indicating the variation of BCD morphology with gradient nanotwin structure. The local density of GNDs associated with this BCD, ρ_G^{BCD} , is estimated as $3.6 \times 10^{14} \text{ m}^{-2}$, and the corresponding average density of GNDs inside grain, ρ_G^{GNT} , is $6.5 \times 10^{11} \text{ m}^{-2}$. The density of dislocations in BCDs is also analyzed from TEM images. These GNDs associated with BCDs serve to accommodate the plastic strain gradient arising from the structural gradient in GNT Cu. Moreover, they can contribute to the sample-level back stress, as to be discussed next.

In addition, the dislocation types inside BCDs are analyzed in terms of mode I, II and III (Lu et al., 2017) using a two-beam diffraction technique in TEM. As illustrated in Fig. 10c, we identify dislocation lines traversing several nanotwin lamellae as mode II dislocations – with slip plane inclined to TBs and Burgers vector parallel to TBs. We also observe BCDs consisting of tangled dislocation lines that can be mode II or mode I – with both the slip plane and Burgers vector inclined to TBs; many dislocation segments near TBs are also observed, and they are either mode II or mode III – with both slip plane and Burgers vector parallel to TBs.

Based on the above results, we separate the strengthening effects in GNT Cu due to various types of dislocations indicated in Fig. 10c. First, the effective stress is controlled by mode II dislocations traversing several twin lamellae. As discussed earlier, the measured effective stresses are almost independent of twin thickness and approach similar saturated values around 100 MPa in both HNT and GNT Cu. The characteristic length scale associated with the effective stress of about 100 MPa can be estimated as $\sim 100 \text{ nm}$, which is two and five times the twin thickness of NT-④ and NT-①, respectively. Hence, such mode II dislocations should consist of connected segments that traverse several nanotwin lamellae, termed trans-twin dislocations (Bu et al., 2023), and move concertedly as a continuous line on the corrugated $\{111\}$ glide plane in those nanotwin lamellae.

Next, we consider the dislocations responsible for the type I back stress arising in HNT Cu that exhibits a strong dependence on twin thickness. This type of back stress can result from the GNDs accumulated at TBs, referred to as GNDs_{HNT}. During plastic deformation, glide dislocations on different slip systems in nanotwins produce deformation incompatibility at TBs. Such incompatibility would lead to overlap or opening if adjacent nanotwin lamellae are allowed to deform independently (Fig. 10d). To accommodate the incompatibility, GNDs_{HNT} of mode I can be accumulated at TBs (Fig. 10e). Their density ρ_G^{HNT} should scale with $\Delta\gamma^p / (\lambda b)$, where $\Delta\gamma^p$ is the local incompatible strain at a TB. Hence, the back stress associated with ρ_G^{HNT} in HNT Cu will increase with decreasing twin thickness. Note that the same kind of back stress can arise from the locally homogeneous nanotwins in GNT Cu as well.

Finally, we consider the dislocations responsible for the type II back stress that increases with structural gradient in GNT Cu. The BCDs represent a new type of heterogeneous dislocation structure. A typical BCD appears to consist of tangled dislocation lines of modes I and II traversing several nanotwin lamellae (Fig. 10c). These dislocations can act as forest obstacles to facilitate the accumulation of GNDs, referred to as GNDs_{GNT}, at this BCD, which produce an effective misorientation across the BCD, as illustrated in Figs. 10f and g. More specifically, the yield strength gradient of a GNT sample under tension generates a gradient distribution of plastic strains. Such gradient plastic strains are similar to those developed in a bent beam where the top/bottom-surface region has a larger plastic strain than the neutral-plane region in the middle of the beam. In both cases, GNDs are needed to accommodate the lattice curvature associated with gradient plastic strains (Fig. 10f), and these GNDs should be the edge dislocations with both Burgers vector and dislocation line vector residing in the bent lattice planes. These bent planes correspond to the $\{111\}$ slip planes parallel to TBs in GNT samples. Hence, the most efficient dislocation GND configurations in GNT Cu should consist of mode III dislocations (Fig. 10g), which could result from the reaction products of mode I and mode II dislocations with TBs. Based on the previous analysis of back stress for conventional dislocation cell structures (Mughrabi, 1983), the GNDs_{GNT} in BCDs could play a similar role in dislocation cell walls and thus produce long-range, directional back stresses to hinder dislocation glide in between BCDs. It follows that local back stresses could collectively result in the sample-level extra back stress measured from GNT Cu. This analysis is supported by the fact that the measured effective density of GNDs associated with BCDs, denoted as ρ_G^{GNT} , matches the gradient of plastic strain arising from the structural gradient in GNT Cu.

6. Summary and outlook

We have presented a comprehensive report for recent studies of the mechanics of gradient nanostructured metals, focusing on GNT Cu as a model system, to understand the extra strengthening effect of structural gradients and resultant plastic strain gradients. These integrated experimental and modeling studies have unveiled the spatiotemporal evolution of both plastic strain gradients and extra back stresses originating from structural gradients. Direct connections are established between the extra strength of GNT Cu at the sample level and the synergistic strengthening effects induced by local nanotwin structures and their gradients.

In particular, we have emphasized the relationships between different types of back stresses induced by heterogeneous nanotwin structures when employing various RVE sizes. The back stress within a large RVE, such as that found in the GNT sample, represents an average over the back stresses associated with all small RVEs within the large RVE. Each small RVE encompasses two distinct types of back stress: type I, stemming from structural heterogeneity within small RVEs containing nanotwins with uniform thickness; type II, arising from nanotwin thickness gradients across RVEs. A comprehensive understanding and quantification of these relationships, as demonstrated for GNT Cu, are crucial for the design and optimization of structural gradients in gradient nanostructured metals, thereby enhancing the resultant extra strengthening effect.

Moreover, we have developed and validated the p-SGP and m-SGP models based on systematic experimental studies of GNT Cu.

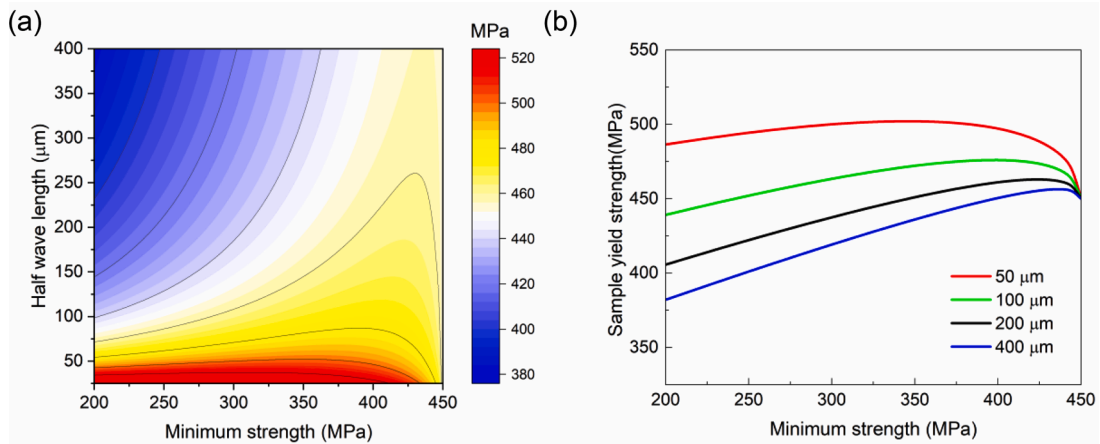


Fig. 11. Optimization of the sample-level yield strength by tuning the minimum local strength and wave length, while the maximum local strength is fixed (Zhang et al., 2020). (a) Contour plot of the sample-level yield strength, when the maximum local strength is fixed at 446 MPa. (b) Representative curves of the sample-level yield strength versus minimum local strength extracted from (a) for several half wave lengths.

They effectively capture gradient plasticity-induced strengthening effects while facilitating numerical solutions by obviating the need for higher-order stress-related quantities. These lower-order gradient models can be extended for investigating the mechanics of gradient nanostructured metals in the future.

To provide an outlook on future research directions in the mechanics of gradient nanostructured metals, and, more broadly, HNMs, we offer below examples of utilizing the SGP models and insights from GNT Cu to evaluate and enhance the strengthening effects of different types of heterogeneous nanostructures.

6.1. Design of optimal GNT structures

For the study of GNT Cu, an overarching goal is to integrate experimental and theoretical efforts to enhance the extra strengthening effects of heterogeneous nanostructures by deepening plastic strain gradients. For example, we have explored optimizing initial distributions of plastic flow resistance in GNT Cu (Zhang et al., 2020). When considering triangle-wave distributions, key parameters to control include the maximum and minimum values of initial yield strength, along with the wave length. It should be noted that certain regions within the parameter space may not be accessible due to limitations imposed by material processing. For example, while reducing twin thickness can raise local strength, maintaining a stable nanotwin structure by electrodeposition present challenges for continuous reduction. Recognizing this constraint, we assume a fixed maximum local strength and then adjust the minimum local strength and wave length to seek the optimal sample-level yield strength based on the p-SGP model in Section 4.

Fig. 11a shows the contour plot of the predicted sample-level yield strength of GNT Cu within the parameter space of the minimum local strength and the half wave length $\lambda/2$, when keeping the maximum local strength at 446 MPa, which is the highest local yield strength in the GNT-4 model. It is seen that the optimized sample-level yield strength occurs at the smallest $\lambda/2$ and an intermediate minimum yield strength. This result can be rationalized by recognizing that the optimal sample-level yield strength is governed by the collective effects of increased mean value and gradient of local strengths. When the maximum local strength is fixed, an increase of the minimum local strength with a concomitant decrease of $\lambda/2$ can counteract each other, limiting the enhancement of the sample-level yield strength.

Extracted from Fig. 11a, the predicted curves of the sample-level yield strength versus minimum local strength are plotted for representative values of $\lambda/2$ in Fig. 11b. Across these curves, the sample-level yield strength exceeds the maximum local strength. Moreover, the non-monotonic change of the sample-level yield strength with the minimum local strength becomes more pronounced as $\lambda/2$ decreases to 100 μm or less. Notably, the optimized sample-level yield strength exceeds that of the GNT-4 model, 490 MPa, with a minimum local strength of 223 MPa. This analysis indicates that the strength of the experimental GNT-4 sample could be further elevated if its minimum local strength were to increase from 223 MPa to around 350 MPa. In the future, integrated experimental and modeling studies are needed to further explore the design of optimal GNT structures.

6.2. Strengthening by large plastic strain gradients

The p-SGP and m-SGP models developed for GNT Cu can be extended to investigate the strengthening effect of plastic strain gradient in other material systems under different loading conditions. In this paper, we present the formulation and application of p-SGP and m-SGP models for studying gradient plastic deformation resulting from the structural gradient and associated strength gradient in GNT Cu. During uniaxial tension, the axial strain is uniform in the sample cross section of GNT Cu. As shown in Fig. 3, once progressive yielding is completed, the plastic strain gradient reaches saturation, as dictated by the strength gradient. It follows that the extra strength arising from the plastic strain gradient reaches saturation. The analysis in Section 6.1 provides initial design

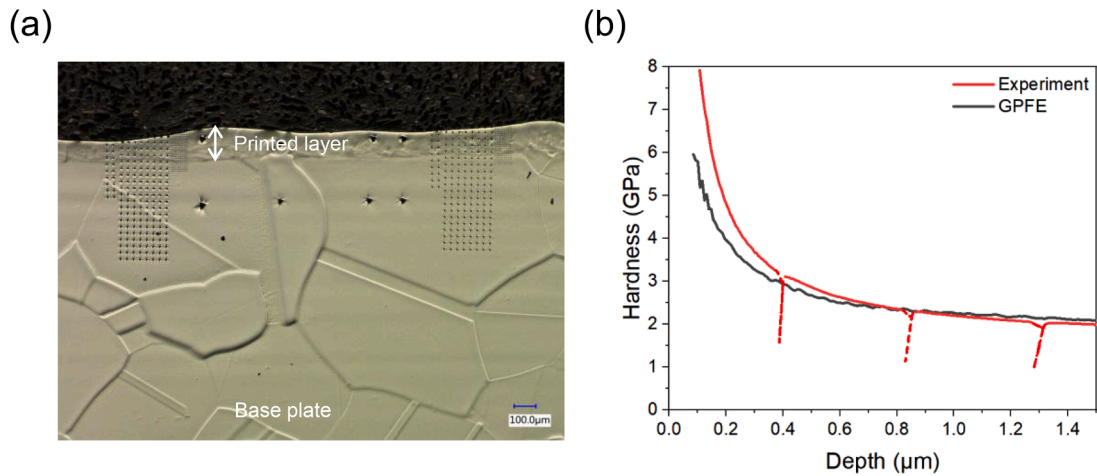


Fig. 12. Experiment and modeling of nanoindentation of printed stainless steel (Ding et al., 2021). (a) Optical micrograph showing nanoindentation arrays on a longitudinal section of a laser single-track printed layer on a baseplate with giant grains. (b) Comparison of nanoindentation hardness of the printed layer versus depth curves between experiments and gradient plasticity finite element (GPFE) simulations based on the p-SGP model. Red dashed lines represent unloading segments in experiments.

considerations for gradient nanostructures to deepen the saturated gradient of plastic strain and thereby enhance the overall strengthening effect. Practically, the attainable plastic strain gradient due to a built-in structural gradient can be limited by the range of thermomechanical conditions accessible by a specific processing method. In contrast, large plastic strain gradients can develop in problems such as beneath a nanoindenter, near a sharp notch, within twisted wires, etc. (Fleck et al., 1994). For these problems, a small RVE can be used to analyze large plastic strain gradients and their strengthening effects. To achieve this, the p-SGP and m-SGP models can simplify numerical solutions, since they belong to lower-order gradient theory and thus eliminate the need for higher-order stress-related quantities.

As an example, we briefly present the application of the p-SGP model for the study of nanoindentation of laser-melted stainless steel single tracks (Ding et al., 2021). A single-track layer of 316L stainless steel is processed from laser powder bed fusion to serve as a model sample configuration (Birnbaum et al., 2020). This single-track layer is made on a 5 mm thick 316L baseplate with a grain size of $\sim 400 \mu\text{m}$. Since the printed layer has a tendency of epitaxial growth from the baseplate, its grain characteristics, including grain size and orientation, largely follow those of the baseplate (Fig. 12). The grains in the single-track layer contain a number of printing-induced dislocation cells of a few hundred nanometers in size, elevating both the yield strength and the rate of work hardening of as-printed materials.

As shown in Fig. 12a, nanoindentation tests are performed on the polished side surface of both the baseplate and printed layer. Fig. 12b displays the representative nanoindenter force versus depth response in the printed layer, which is affected by grain sizes in the baseplate and printed layer as well as sub-structural features arising from additive manufacturing, such as printing-induced dislocation cells. We use the p-SGP model (Zhang et al., 2020) to perform 3D finite element simulations of size-dependent nanoindentation behavior. The gradient-dependent plastic parameters in Eq. (3), including κ , ε_2 and n_2 , are determined through matching the simulation and experimental results of size-dependent nanoindentation behavior at small indentation depths. The simulated indentation force versus depth curves agree with the corresponding experimental curves. Based on these results, the derived indentation hardness versus depth curve agrees with the corresponding experimental curve (Fig. 12b). Hence, the p-SGP model enables the quantitative investigation of size-dependent nanoindentation hardness when the indentation depths are greater than $\sim 0.2 \mu\text{m}$. A different effect of size-dependent nanoindentation arises at smaller indentation depths, since plastic flow is controlled by dislocation nucleation and cannot be represented by the same set of plastic parameters in the p-SGP model. The dashed lines in Fig. 12b indicate nanoindentation unloading segments in experiments, which are not simulated in this work and warrant further modeling studies in the future.

6.3. Mechanics of HNMs

Understanding the mechanics of HNMs poses significant challenges due to the presence of multiple nanostructure length scales, resulting in complex strengthening effects from various types of heterogeneous nanostructures. The layered gradient structure of GNT Cu provides a simplified quasi-one-dimensional model system for understanding the mechanics of HNMs. An important insight gained from thorough investigations of GNT Cu is the impact of the RVE size on capturing different types of back-stress strengthening effects. Once a constitutive model of GNT Cu is established and calibrated using a specific RVE size, caution should be taken when applying the model to evaluate and optimize the strengthening effect of GNT Cu through, for example, finite element simulations. This is because a change in the element size may correspond to a change in the RVE size, necessitating an adjustment of the back stresses represented by the RVE.

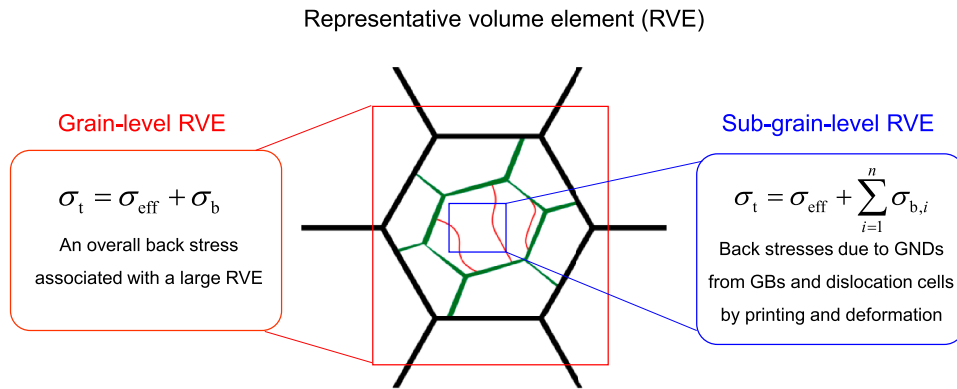


Fig. 13. A unified conceptual framework on the mechanics of HNMs based on grain-level and sub-grain-level RVEs. Black, green and red lines represent GBs, dislocation cells induced by printing and deformation, respectively.

Insight into the RVE size effect on GNT Cu has broad implications for studying the mechanics of HNMs, particularly those with strong nanostructure heterogeneities leading to significant plastic strain gradients. For example, additively manufactured 316L stainless steel typically features printing-induced chemical and dislocation cells (about 0.5 μm in size) within grains (tens of microns in size) (Wang et al., 2018). As illustrated in the left panel of Fig. 13, a grain-level RVE encompassing a representative grain is associated with a grain-level back stress, which represents an average of back stresses associated with all sub-grain-level RVEs within the grain (Chen et al., 2019; Zhang et al., 2022). These sub-grain-level back stresses, as illustrated in the right panel of Fig. 13, can originate from GNDs generated from grain boundaries and dislocation cells due to printing and straining experiments. These GNDs, spanning across and within sub-grain-level RVEs, evolve with increasing load, leading to the evolution of the sub-grain-level back stresses. Similar to the case of GNT Cu, caution should be taken when applying a constitutive model calibrated by a specific RVE size. This underscores the inherent complexity in evaluating and enhancing the strengthening effects from different types of heterogeneous nanostructures to achieve outstanding mechanical properties of HNMs.

The above outlook highlights only a few among the numerous potentially fascinating avenues for future research on HNMs. With ongoing progress in material processing, characterization, and modeling, we anticipate remarkable strides in understanding the mechanics of HNMs. These advancements will further enhance the strengthening effects of heterogeneous nanostructures, ultimately unlocking their full potential.

CRediT authorship contribution statement

Yin Zhang: Writing – original draft, Software, Methodology, Investigation, Conceptualization. **Zhao Cheng:** Methodology, Investigation, Writing – original draft. **Ting Zhu:** Writing – review & editing, Writing – original draft, Supervision, Methodology, Conceptualization. **Lei Lu:** Writing – review & editing, Supervision, Conceptualization, Funding acquisition.

Declaration of competing interest

The authors declare that they have no known competing financial interests or personal relationships that could have appeared to influence the work reported in this paper.

Data availability

Data will be made available on request.

Acknowledgments

We sincerely thank Profs. Huajian Gao and HengAn Wu and Dr. Linfeng Bu for their collaborative work on GNT Cu. L.L. acknowledges financial support from the National Natural Science Foundation of China (NSFC, Grant Numbers. 51931010, 92163202); the project of Global Common Challenges (172GJHZ2023075GC), Chinese Academy of Sciences (CAS). Z.C. acknowledges financial support from NSFC under Grant Numbers. 52371124 & 52001312 and Youth Innovation Promotion Association, CAS.

References

- Aifantis, E.C., 1984. On the microstructural origin of certain inelastic models. *J. Eng. Mater. Technol. Trans. ASME* 106, 326–330.
 Ashby, M.F., 1970. The deformation of plastically non-homogeneous materials. *Philos. Mag.* 21, 399–424.

- Bassani, J.L., 2001. Incompatibility and a simple gradient theory of plasticity. *J. Mech. Phys. Solids* 49, 1983–1996.
- Birnbaum, A.J., Ryou, H., Steuben, J.C., Iliopoulos, A.P., Wahl, K.J., Michopoulos, J.G., 2020. Nested size effects in the nanoindentation response of additively manufactured 316L stainless steel. *Mater. Lett.* 280, 128570.
- Bower, A.F., 2009. *Applied Mechanics of Solids*. CRC Press, Boca Raton, Florida, USA.
- Bu, L., Cheng, Z., Zhang, Y., Wu, H., Zhu, T., Lu, L., 2023. Trans-twin dislocations in nanotwinned metals. *Scr. Mater.* 229, 115348.
- Chen, W., Voisin, T., Zhang, Y., Forien, J.-B., Spadaccini, C.M., McDowell, D.L., Zhu, T., Wang, Y.M., 2019. Microscale residual stresses in additively manufactured stainless steel. *Nat. Commun.* 10, 4338.
- Cheng, Z., Bu, L., Zhang, Y., Wu, H., Zhu, T., Gao, H., Lu, L., 2022. Unraveling the origin of extra strengthening in gradient nanotwinned metals. *Proc. Natl. Acad. Sci.* 119, e2116808119.
- Cheng, Z., Bu, L., Zhang, Y., Wu, H., Zhu, T., Lu, L., 2023. Characterization of gradient plastic deformation in gradient nanotwinned Cu. *Acta Mater.* 246, 118673.
- Cheng, Z., Zhou, H., Lu, Q., Gao, H., Lu, L., 2018. Extra strengthening and work hardening in gradient nanotwinned metals. *Science* 362, eaau1925.
- Dickson, J.I., Boutin, J., Handfield, L., 1984. A comparison of two simple methods for measuring cyclic internal and effective stresses. *Mater. Sci. Eng.* 64, L7–L11.
- Ding, K., Zhang, Y., Birnbaum, A.J., Michopoulos, J.G., McDowell, D.L., Zhu, T., 2021. Strain gradient plasticity modeling of nanoindentation of additively manufactured stainless steel. *Extreme Mech. Lett.* 49, 101503.
- Fleck, N.A., Muller, G.M., Ashby, M.F., Hutchinson, J.W., 1994. Strain gradient plasticity - theory and experiment. *Acta Metall. Mater.* 42, 475–487.
- Gao, S., Li, Z., Van Petegem, S., Ge, J., Goel, S., Vas, J.V., Luzin, V., Hu, Z., Seet, H.L., Sanchez, D.F., Van Swyghenoven, H., Gao, H., Seita, M., 2023. Additive manufacturing of alloys with programmable microstructure and properties. *Nat. Commun.* 14, 6752.
- Gudmundson, P., 2004. A unified treatment of strain gradient plasticity. *J. Mech. Phys. Solids* 52, 1379–1406.
- Guo, X., Zhang, J., Kong, T., Mao, N., Sun, C., Cui, Y., Xiong, Z., 2024. Understanding extra strengthening in gradient nanotwinned Cu using crystal plasticity model considering dislocation types and strain gradient effect. *Int. J. Plast.* 172, 103822.
- Ji, W., Zhou, R., Vivegananthan, P., See Wu, M., Gao, H., Zhou, K., 2023. Recent progress in gradient-structured metals and alloys. *Prog. Mater. Sci.* 140, 101194.
- Lele, S.P., Anand, L., 2008. A small-deformation strain-gradient theory for isotropic viscoplastic materials. *Philos. Mag.* 88, 3655–3689.
- Li, X.Y., Wei, Y.J., Lu, L., Lu, K., Gao, H.J., 2010. Dislocation nucleation governed softening and maximum strength in nano-twinned metals. *Nature* 464, 877–880.
- Lu, K., 2016. Stabilizing nanostructures in metals using grain and twin boundary architectures. *Nat. Rev. Mater.* 1, 16019.
- Lu, K., Lu, L., Suresh, S., 2009a. Strengthening Materials by Engineering Coherent Internal Boundaries at the Nanoscale. *Science* 324, 349–352.
- Lu, L., Chen, X., Huang, X., Lu, K., 2009b. Revealing the maximum strength in nanotwinned copper. *Science* 323, 607–610.
- Lu, Q., You, Z., Huang, X., Hansen, N., Lu, L., 2017. Dependence of dislocation structure on orientation and slip systems in highly oriented nanotwinned Cu. *Acta Mater.* 127, 85–97.
- Ma, E., Zhu, T., 2017. Towards strength–ductility synergy through the design of heterogeneous nanostructures in metals. *Mater. Today* 20, 323–331.
- Mughrabi, H., 1983. Dislocation wall and cell structures and long-range internal-stresses in deformed metal crystals. *Acta Metall.* 31, 1367–1379.
- Niordson, C.F., Hutchinson, J.W., 2003. On lower order strain gradient plasticity theories. *Eur. J. Mech. A. Solids* 22, 771–778.
- Nix, W.D., Gao, H.J., 1998. Indentation size effects in crystalline materials: a law for strain gradient plasticity. *J. Mech. Phys. Solids* 46, 411–425.
- Ren, J., Zhang, Y., Zhao, T., Chen, Y., Guan, S., Liu, Y., Liu, L., Peng, S., Kong, F., Poplawsky, J.D., Gao, G., Voisin, T., An, K., Wang, Y.M., Xie, K.Y., Zhu, T., Chen, W., 2022. Strong yet ductile nanolamellar high-entropy alloys by additive manufacturing. *Nature* 608, 62–68.
- Wang, Y.M., Voisin, T., McKeown, J.T., Ye, J.C., Calta, N.P., Li, Z., Zeng, Z., Zhang, Y., Chen, W., Roehling, T.T., Ott, R.T., Santala, M.K., Depond, P.J., Matthews, M.J., Hamza, A.V., Zhu, T., 2018. Additively manufactured hierarchical stainless steels with high strength and ductility. *Nat. Mater.* 17, 63–70.
- Wu, X., Zhu, Y., 2017. Heterogeneous materials: a new class of materials with unprecedented mechanical properties. *Mater. Res. Lett.* 5, 527–532.
- You, Z., Li, X., Gui, L., Lu, Q., Zhu, T., Gao, H., Lu, L., 2013. Plastic anisotropy and associated deformation mechanisms in nanotwinned metals. *Acta Mater.* 61, 217–227.
- Zhang, Y., Cheng, Z., Lu, L., Zhu, T., 2020. Strain gradient plasticity in gradient structured metals. *J. Mech. Phys. Solids* 140, 103946.
- Zhang, Y., Ding, K., Gu, Y., Chen, W., Wang, Y.M., El-Awady, J., McDowell, D.L., Zhu, T., 2022. Modeling of microscale internal stresses in additively manufactured stainless steel. *Modell. Simul. Mater. Sci. Eng.* 30, 074001.
- Zhu, T., Gao, H.J., 2012. Plastic deformation mechanism in nanotwinned metals: an insight from molecular dynamics and mechanistic modeling. *Scr. Mater.* 66, 843–848.
- Zhu, Y., Ameyama, K., Anderson, P.M., Beyerlein, I.J., Gao, H., Kim, H.S., Lavernia, E., Mathaudhu, S., Mughrabi, H., Ritchie, R.O., Tsuji, N., Zhang, X., Wu, X., 2021. Heterostructured materials: superior properties from hetero-zone interaction. *Mater. Res. Lett.* 9, 1–31.
- Zhu, Y., Wu, X., 2023. Heterostructured materials. *Prog. Mater. Sci.* 131, 101019.